Size, Diffusion and Sedimentation of Gold Nanorods.

Susanne Seibt[a,b,c,*], Joseph Pearson[d], Reece Nixon-Luke[e], Heyou Zhang[b], Peter R. Lang[f], Gary Bryant[e], Helmut Cölfen[d], Paul Mulvaney[b]

[a] *SAXS / WAXS Beamline, Australian Synchrotron, ANSTO, 800 Blackburn Road, VIC-3168 Clayton, Australia.*
[b] *ARC Centre of Excellence in Exciton Science, School of Chemistry, The University of Melbourne, Parkville, VIC 3010, Australia.*
[c] *Physical Chemistry I, University of Bayreuth, Universitätsstraße 30, 95448 Bayreuth, Germany*
[d] *Physical Chemistry, University of Konstanz, Universitätsstraße 10, 78457 Konstanz, Germany.*
[e] *School of Science, RMIT University, VIC-3038 Melbourne, Australia.*
[f] *Institute of Biomacromolecular Systems and Processes, Research Centre Jülich, 52425 Jülich, Germany.*
[*] Email: susanne.seibt@unimelb.edu.au

Abstract

We have used four different analytical techniques (electron microscopy (TEM), dynamic light scattering (DLS), analytical ultracentrifugation (AUC) and small angle X-rays scattering (SAXS) to measure the length and width as well as the diffusion coefficients of gold nanorods (GNR) of different aspect ratio. All four methods could reproduce the trends in aspect ratio and both length and width could be extracted once the ligand shell was accounted for. The CTAB bilayer coating was determined to have a thickness of 3.34, 3.02 and 3.26 nm by SAXS, DLS and AUC respectively. TEM nevertheless yielded the best predictions for the nanorod ensemble surface plasmon resonance using COMSOL simulations. All four methods yielded better fits when the rods were treated as spherically capped cylinders.

1 Introduction

It is well known that surface plasmon resonances (SPR) in metal nanocrystals are highly sensitive to both particle shape and size and that nanocrystals with different morphologies exhibit different photochemical reactivity[1,2]. For many applications it would be highly useful to be able to predict the SPR band position from histograms of the particle size and shape distribution. This would ultimately enable real-time monitoring of important steps in nanocrystal growth such as symmetry breaking and facet ripening[3].

For inorganic materials containing high atomic number elements, transmission electron microscopy (TEM) remains the method of choice for particle sizing because it allows atomic resolution, as well as both size and shape distributions to be determined. Nowadays, the detailed characterisation of single nanocrystal dimensions is possible and even single atom counting in favourable cases.[4] However, TEM interrogates only a small sample volume and a limited number of observer selected particles. Therefore, impractically large sample populations may be needed to obtain valid statistical distributions (see discussion in Schöpe et al.[5] and Eitel et al.[6]). In addition, the measured dimensions are those in the dried state, and supplementary information about coatings and ligands is lost.[7,8]

For larger particle dimensions spanning from a couple of nanometers to about 1 micron, scattering techniques are typically employed such as Dynamic Light Scattering (DLS), Small Angle X-ray Scattering (SAXS), or Small Angle Neutron Scattering (SANS). DLS is based on the hydrodynamic behaviour of the ensemble, i.e. measurement of the diffusion coefficient. The hydrodynamic size is then inferred from the Stokes-Einstein-Sutherland (SES) equation[9,10]. Combining polarised and depolarised scattering measurements enables the determination of the hydrodynamic behaviour of nanorods and their size determination in situ. For anisotropic particles, the presence of a depolarised component in the scattered light enables the determination of both translational (D_t) and rotational (D_r) diffusion coefficients. Hence, depolarised dynamic light scattering (DDLS) can be used to determine not only the hydrodynamic radius of the equivalent sphere but also the actual length and diameter of the diffusing nanorods in solution.[7,8,11,12] However, the final calculation of particle dimensions from the correlation function through DLS experiments is strongly dependent on the model used for the particle shape, which must be known a priori. The utility of the technique is shown by recent work in which it was demonstrated that the particle shape of PNIPAM coated nanorods changes from prolate spheroid to cylindrical with increasing

temperature as the PNIPAM shell collapses.[13]

Other techniques such as size exclusion chromatography enable separation of different sized gold nanocrystals[14] but do not allow absolute determination of particle dimensions. Another potentially valuable technique is analytical ultracentrifugation (AUC). Ironically, AUC was originally developed to prove the nanoscale dimensions of the particles in ruby red gold colloids. Modern instruments can detect very small changes in diameter of spherical particles but while this technique has excellent size resolution, it is unclear how well it can resolve aspect ratio differences in a population of nanorods. There have been only a few AUC studies of anisotropic nanoscale particle systems thus far[15–20] and the focus has been on high aspect ratio materials, although there has been considerable investigation of spherical nanocrystals[21,22]. Importantly, AUC also determines particle size through the SES equation.

SAXS provides an alternative method for particle sizing. SAXS is generally a synchrotron based method although some high intensity sources are now available in the lab. SAXS works better for high Z materials and can also resolve both particle size and shape down to 1 nm in diameter[23,24]. It works well on dilute samples and whilst often employed to resolve self-assembled colloid structures, it can be used to analyse the morphology of single particles as well. It suffers from the same limitations as other scattering methods, in that the particle morphology should be known a priori although it is possible to do model independent fitting under some circumstances. There is a risk that during prolonged irradiation the intense X-ray beam will alter the morphology of the particles. Importantly, both SAXS and AUC can resolve the contributions from surfactant layers as well as the core, which is a distinct advantage over DLS and TEM. A significant advantage of SAXS alone is that it can provide time resolved nanocrystal growth kinetics.[3 23,24].

A priori it is unclear which of the methods outlined above is best suited to anisotropic nanocrystal sizing. Each of the methods has distinct advantages and disadvantages. Hence, in this paper we systematically compare different sizing techniques for a model anisotropic nanocrystal system - gold nanorods. Precise morphology is needed in order to accurately predict the optical properties of these particles, which are extremely sensitive to the particle aspect ratio and end-cap geometry. We compare four techniques (HRTEM, SAXS, DLS, AUC) on a set of 10 gold nanorod samples with different aspect ratios. We stress that we only aim to determine the mean values of the lengths and widths of the gold rods. We do not attempt to measure the actual size distributions. As an independent measure of the accuracy of the data, we use the resultant analytical sizing results to predict the UV-visible extinction spectrum of the rods and compare it to the measured absorption spectra of all samples.

2 Methods

2.1 Synthesis of gold nanorods.

Monodisperse gold nanorods (GNR) were synthesised using a hydroquinone-based seeded-growth method described in detail elsewhere.[3] Briefly, for CTAB-capped seeds, 5mL of aqueous 0.5 mM $HAuCl_4$ and 5mL of 0.2 M aqueous CTAB were mixed and then stirred for 10 min at room temperature. Next, 600 μL of a freshly prepared 0.01 M $NaBH_4$ solution was added quickly under vigorous stirring. After 2 min, the stirring was stopped and the seeds were aged for 1h at room temperature. To grow the rods, 10 mL of a 0.1 M aqueous CTAB solution, 50 μl each of a $HAuCl_4$ solution (with various concentrations) and 0.1 M $AgNO_3$ solution were added and mixed until completely dissolved. To reduce the gold (III) chloride, hydroquinone was added and the growth solution gently mixed until complete decolouration had occurred. Finally, 400 μL of the aged CTAB-capped Au seeds was added and mixed thoroughly. The Au nanorods were grown for 24h at room temperature. The solution was purified by centrifugation (10 min, 14000 rcf) before washing with water twice and redispersing the final nanorods in 2 mL water to yield a concentrated colloid.

2.2 Absorption spectra.

UV-Vis spectra were recorded using an Agilent HP 8453 instrument or a Cary 5000 spectrophotometer (Agilent, USA). The cuvettes used had a 1 cm pathlength.

2.3 Transmission electron microscopy.

TEM images were obtained with a LEO 922 OMEGA EFTEM using an acceleration voltage of 200 kV from Zeiss (Germany). Zero-loss filtered images were recorded with a bottom mounted Ultrascan 1000 (Gatan) CCD camera system. The images were processed with a digital imaging processing system (Gatan Digital Micrograph 3.9 for GMS 1.4). For the TEM analysis, 4 μL of the as-prepared solution was dried on a copper mesh grid

coated with carbon film. For size evaluation, the software ImageJ (version 1.44p, U.S. National Institute of Health) was used.

2.4 Small-angle X-ray scattering.

SAXS experiments were performed on the SAXS/WAXS beamline at the Australian Synchrotron, Melbourne, Australia and employed a 11.5 keV beam with the detector placed 1.6 m distance to the sample. Two-dimensional SAXS patterns were acquired in 1 min time frames with a PILATUS 1 M detector and radially integrated to yield the SAXS intensity I(q) vs. scattering vector q. The unpurified gold nanorod solution was measured in a standard 1mm quartz capillary (Hilgenberg, wall thickness 0.01mm). All measurements were background corrected using a capillary filled with 1 mM CTAB solution. For size evaluation, the samples were fitted using the software "Scatter" [25] and SasView.

The rods were treated as spherically capped cylinders where R is the rod radius and L is the length of the cylinder. The overall length of the particle is therefore $L + 2R$. Previous SAXS analysis has shown that similar gold nanorod samples are best defined and fitted with models where the radius of the spherical end caps matches the radius of the cylinder. [3]

2.4.1 Core Gold Rods.

For a pure gold spherically capped, cylindrical particle, the scattered beam intensity *I(q)* is calculated using

$$I(q) \propto \frac{1}{V_C}\langle A^2(q)\rangle \tag{1}$$

where the amplitude *A(q)* is given by

$$A(q) = \Delta\rho\pi R^2 L \frac{\sin\left(\frac{1}{2}qL\cos\theta\right)}{\frac{1}{2}qL\cos\theta}\frac{2J_1\left(qR\sin\theta\right)}{qR\sin\theta} + \Delta\rho 4\pi R^3\cos\left(\frac{1}{2}qL\cos\theta\right)\left(\frac{\sin qR - qR\cos qR}{(qR)^3}\right) - \tag{2}$$

$$-\Delta\rho 4\pi R^3\sin\left(\frac{1}{2}qL\cos\theta\right)\int_0^1 \sin\left(qRt\cos\theta\right)dt\cdot\left(1-t^2\right)\frac{J_1\left[qR\sin\theta\left(1-t^2\right)^{\frac{1}{2}}\right]}{qR\sin\theta\left(1-t^2\right)^{\frac{1}{2}}}$$

Here the contrast $\Delta\rho = \rho_c - \rho_{solv}$, ρ_c is the scattering length density of the capped cylinder particle and ρ_{solv} is the scattering length density of the solvent. [26] The $\langle ...\rangle$ brackets denote an average of the structure over all orientations. θ represents the angle between the axis of the cylinder and q. $\langle A^2(q)\rangle$ is then the form factor, *P(q)*. The scale factor is equivalent to the volume fraction of cylinders, each of volume V_C. J_1 denotes the first order Bessel function.

The volume of the capped cylinder is

$$V_C = V_{cyl} + V_{sph} = \pi R^2 L + \frac{4}{3}\pi R^3 \tag{3}$$

2.4.2 Core-shell gold nanorods

In the case of a CTAB coated gold rod, which is encountered in practical measurements, it is necessary to account for x-ray scattering by the surfactant.Assuming the shell envelops the entire core particle with a thickness T and a scattering length density ρ_s, the outer radius of the shell is given by $R + T$.

The scattered beam intensity *I(q)* is then calculated using

$$I(q) \propto \frac{1}{V_S}\langle A^2(q)\rangle \tag{4}$$

The amplitude *(A(q)* is given by

$$A(q) = (\rho_c - \rho_s)\pi R^2 L \frac{\sin\left(\frac{1}{2}qL\cos\theta\right)}{\frac{1}{2}qL\cos\theta}\frac{2J_1\left(qR\sin\theta\right)}{qR\sin\theta} + (\rho_c - \rho_s)4\pi R^3\cos\left(\frac{1}{2}qL\cos\theta\right)\left(\frac{\sin qR - qR\cos qR}{(qR)^3}\right) -$$

$$-(\rho_c - \rho_s)4\pi R^3\sin\left(\frac{1}{2}qL\cos\theta\right)\int_0^1 \sin\left(qRt\cos\theta\right)dt\cdot\left(1-t^2\right)\frac{J_1\left[qR\sin\theta\left(1-t^2\right)^{\frac{1}{2}}\right]}{qR\sin\theta\left(1-t^2\right)^{\frac{1}{2}}} +$$

$$+(\rho_s-\rho_{solv})\pi(R+T)^2L\frac{\sin\left(\frac{1}{2}qL\cos\theta\right)}{\frac{1}{2}qL\cos\theta}\frac{2J_1\left(q(R+T)\sin\theta\right)}{q(R+T)\sin\theta}+ \tag{5}$$

$$+(\rho_s-\rho_{solv})4\pi(R+T)^3\cos\left(\frac{1}{2}qL\cos\theta\right)\left(\frac{\sin q(R+T)-q(R+T)\cos q(R+T)}{(q(R+T))^3}\right)-$$

$$-(\rho_s-\rho_{solv})4\pi(R+T)^3\sin\left(\frac{1}{2}qL\cos\theta\right)\int_0^1\sin\left(q(R+T)t\cos\theta\right)dt\cdot\left(1-t^2\right)\frac{J_1\left[q(R+T)\sin\theta\left(1-t^2\right)^{\frac{1}{2}}\right]}{q(R+T)\sin\theta\left(1-t^2\right)^{\frac{1}{2}}}$$

and

$$V_S=\pi(R+T)^2L+\frac{4}{3}\pi(R+T)^3 \tag{6}$$

2.5 Dynamic light scattering.

Experiments were performed on an ALV-5022F light scattering spectrometer at a laser wavelength of 633 nm. Samples were suspended in water with $<100\times10^{-3}$ M CTAB as stabilising agent and measured in a cylindrical glass cuvette (inner diameter 8 mm) (LSI Instruments, Fribourg) held in a scattering vat temperature controlled to 25 ° (Thermo Neslab RTE 10). A Glan–Thompson prism (extinction ratio $>10^5$) was used to select the polarization of the scattered light. DLS measurements of 120 s duration were obtained in vertical-vertical (VV) and vertical-horizontal (VH) modes at scattering angles from 30 ° to 140 ° with an angular step of 10 °.[27] The data was processed using a custom graphic user interface provided by Lang et al.[7].

For the data analysis of the gold nanorods as small particles with cylindrical shape, the intensity autocorrelation functions measured in VV and VH geometry are given by

$$g_2^{VV}(\tau)-1=\beta\left[A^2\exp\left(-\Gamma\tau\right)+2AB\exp\left(-(\Gamma+\frac{\Delta}{2})\tau\right)+B^2\exp\left(-(\Gamma+\Delta)\tau\right)\right] \tag{7}$$

$$g_2^{VH}(\tau)-1=\beta'\exp\left(-(\Gamma+\Delta)\tau\right) \tag{8}$$

where $\Gamma=2D_tq^2$, $\Delta=12D_r$, D_t is the translational and D_r the rotational diffusion coefficient, which depend on q the scattering vector and τ is the delay time. Finally, $A+B=1$, and the parameters β and β' describe the non-ideal dynamical contrast of the DLS setup. Utilising the numerical approximation for cylinders with flat ends derived by Ortega and de la Torre[28], the diffusion coefficients can be written as:

$$D_t=\frac{k_BT\left(\ln\left(\frac{L}{W}\right)+C_t\right)}{3\pi\eta L} \tag{9}$$

$$D_r=\frac{3k_BT\left(\ln\left(\frac{L}{W}\right)+C_r\right)}{\pi\eta L^3} \tag{10}$$

Here C_t and C_r are second-order polynomials in $\frac{W}{L}$, the coefficients of which have been determined by fitting of numerical data for aspect ratios covering the range $2<\frac{L}{W}<20$[28].

$$C_t=0.312+0.565\frac{W}{L}-0.100\left(\frac{W}{L}\right)^2 \tag{11}$$

$$C_r=-0.662+0.917\frac{W}{L}-0.005\left(\frac{W}{L}\right)^2 \tag{12}$$

Given the aspect ratios determined by our TEM measurements, this approximation is well suited to our samples.

2.6 Analytical Ultracentrifugation.

In an analytical ultracentrifuge (AUC), particles are subjected to a centrifugal field due to the angular velocity, ω of the rotor, and will redistribute in a sample cell according to their size, shape and mass. AUC cells confine the samples to a channel between two windows, and the concentration distribution is dynamically tracked by means of an optical system. The dynamics of a particle in an AUC can be described by a simple mechanical model relating the sedimentation, buoyant and frictional forces. The sedimentation coefficient, S is the ratio of the steady-state particle velocity, u, to the centrifugal field, $\omega^2 r$, where r is the rotor length at the sample. This basic relationship is known as the Svedberg equation, shown in the simplified form of equation 13 and is the fundamental underpinning of the AUC method.

$$S \equiv \frac{u}{\omega^2 r} = \frac{V_p \left(\rho_p - \rho_S\right)}{f} \tag{13}$$

Here V_p is the particle volume and ρ_p and ρ_S are the particle and solvent mass densities respectively and f is the friction coefficient. Derivation by way of this simple mechanical model provides an intuitive understanding of the basic physical process. However, the same result can be gleaned via a rigorous thermodynamic treatment and is robust to end-effects of the particle shape of the friction coefficient.[29]

The experiments were performed in a multiwavelength AUC with the same parameter settings as the GNR experiments reported in[22]. Sedimentation coefficient distributions were extracted from the experimental data using the Wide Distribution Analysis (WDA) algorithm in SedAnal. g(s) analysis methods that ignore diffusion were appropriate for fast sedimenting particles but conversely, this did not allow direct recovery of reliable diffusion coefficients. The measured Svedberg values were converted to standard conditions of water at 20°C, (S20,W).[22]

2.7 COMSOL simulations.

The simulations were carried using the Radio Frequency (RF) module (Electromagnetic Waves, Frequency Domain, (emw)) of COMSOL in 3D geometry. The geometry of the model is shown in Figure S1 and shows the two main domains used in the simulations. The outer domain in grey is the perfectly matched layer (PML), which generally is used in numerical simulations for absorbing waves without back reflection. The inner body in blue constitutes the physical domain and contains a gold nanoparticle and the surrounding environment. The size of the entire model is illustrated separately as both a "front view" and "top view" in figures S1b and S1c respectively. The geometry of the gold nanorod (Figure S1d) is a hemispherically capped cylindrical rod with input length (L) and width (W). The gold nanorod is located in the middle of the physical domain. Further details are provided in the SI.

3 Results and Discussion

3.1 Gold Nanorod Analysis.

The nanoparticles prepared as monodisperse gold nanorods were measured using absorption spectroscopy, transmission electron microscopy (TEM), small angle X-ray scattering (SAXS), dynamic light scattering (DLS) and analytical ultracentrifugation (AUC). The samples were measured under different conditions (dry and in solution). The actual sizes obtained were therefore technique-dependent and influenced by substances adsorbed on the surface of the particle (CTAB). We discuss each set of measurements in turn and tabulate the key data sets (mean length, width, aspect ratio and errors) associated with each. Finally as a method of comparison, we show how well each set of particle distributions predicts the experimentally determined surface plasmon resonance. This is done by using the mean values as input into COMSOL to numerically determine the extinction peak wavelength, which we then compare to the measured peak wavelength.

3.2 TEM Measurements.

TEM images of all ten samples are shown in Figure 1. The average sizes (and standard deviations) reflect the gold core size as surfactants were not resolved in these images.

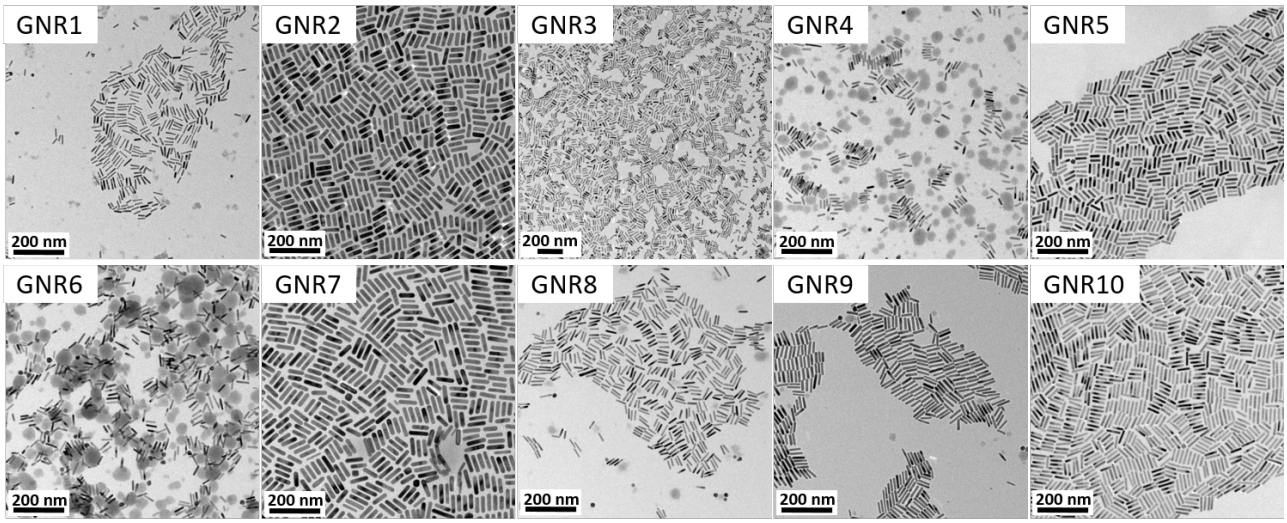

Figure 1: TEM images of the purified gold nanorod solutions GNR1 to GNR10. All nanorod solutions show relatively low concentrations of gold spheres. TEM samples were prepared on carbon grids and images collected at 200 kV. 100 particles per sample were counted to achieve dimensions and standard distributions. The scale bar is 200 nm in all images.

The actual lengths and widths of the gold nanorods were determined using ImageJ software. 100 particles were evaluated for each sample to determine both dimensions of the gold nanorods, as well as the percentage of gold nanospheres in the synthesis solution. From these measurements of the lengths and widths, size distribution histograms were created to calculate the mean size and standard deviation for each data set. The average dimensions, standard deviations and percentage of nanorods are shown in Table 1.

Table 1: The dimensions of the gold rods in samples GNR1 to GNR10 (length, L, width, W, and aspect ratio, AR) as determined from TEM images, including standard deviations and percentage of rods (NR) and spheres (NS) in each sample. 100 particles were counted to calculate dimensions and standard distributions.

Sample ID	**NR %**	**L [nm]**	σ_L **[nm]**	**W [nm]**	σ_W **[nm]**	**AR**
GNR1	77 %	28.39	± 4.49	7.47	± 0.82	3.80
GNR2	93 %	52.80	± 6.07	14.68	± 1.38	3.60
GNR3	56 %	42.17	± 5.33	9.90	± 0.81	4.26
GNR4	74 %	36.40	± 5.11	7.90	± 0.76	4.60
GNR5	88 %	42.75	± 4.29	10.63	± 0.86	4.02
GNR6	83 %	42.93	± 5.64	8.28	± 0.82	5.18
GNR7	99 %	71.98	± 7.31	17.05	± 1.01	4.22
GNR8	89 %	40.09	± 4.42	8.16	± 0.77	4.91
GNR9	91 %	48.54	± 6.87	9.35	± 0.79	5.19
GNR10	88 %	50.27	± 5.66	9.77	± 0.64	5.15

Sample GNR3 contained by far the largest fraction of gold spheres, based on the TEM images. All of the other samples had more than 74% gold nanorods while some samples such as GNR2, GNR7 and GNR9 consisted almost exclusively of gold nanorods, as ascertained from TEM image analysis. These three samples also contained the longest gold nanorods synthesised, which was advantageous for purification by centrifugation. The TEM images of samples GNR4 and GNR6 showed residues from CTAB, which are visible as darker patches around the gold nanorods. The LSPR peak increased in wavelength for samples GNR1 to GNR 10 but, as will be shown, this did not correlate with an increase in actual aspect ratio in all cases. The absolute nanorod dimensions were also important.

3.3 SAXS Measurements.

Small angle X-ray scattering is a versatile method for the characterisation of nanomaterials. Based on the intensity distribution of the scattered X-ray photons, measurements can provide information about the size, size distribution, morphology, crystallinity and agglomeration of samples in solutions. As it probes a very large number of nanoparticles simultaneously, the data gives statistically relevant averages over a large part of the

sample. SAXS is a nondestructive method, without the need for large sample volumes or extensive sample preparation, which makes it ideal for the study of colloidal systems. We used SAXS to determine the lengths and widths of the rods, as well as the thickness of the CTAB surfactant layer on the rod surface.

The collected SAXS data and model fits for each of the unpurified solutions GNR1 to GNR10 are displayed in Figure 2. Each sample is shown separately as a double-logarithmic plot of absolute scattering intensity against the scattering vector q in inverse Å. For all curves the best fitting model was determined to be a "homogeneous core - inhomogeneous shell spherically capped cylinder" as given by eq.5. From these fits, the length, L, the radius, R, the width W = 2·R, and the thickness of the CTAB surfactant shell could all be determined. The extracted values are shown in Table 2.

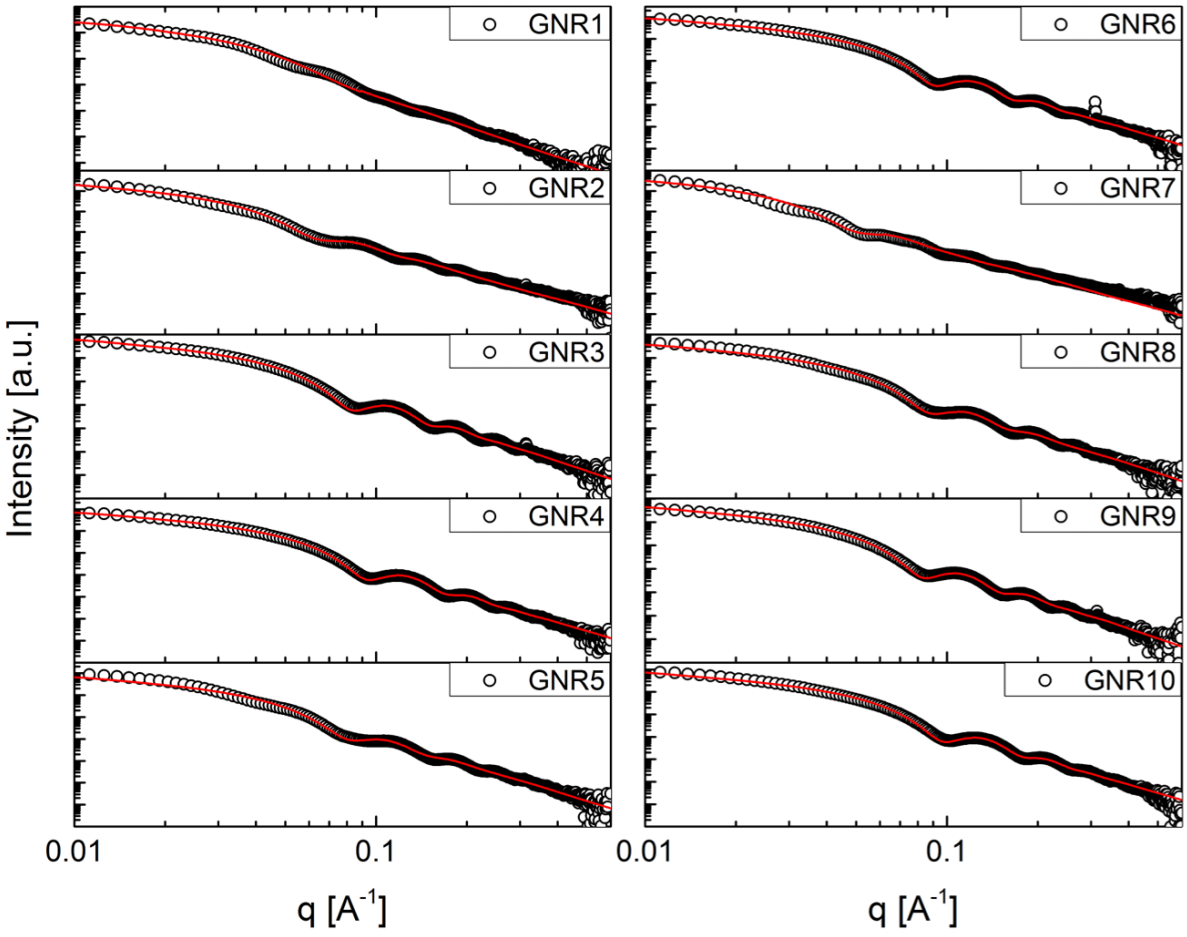

Figure 2: SAXS intensity as a function of scattering vector q for unpurified sample solutions GNR1 (top left) to GNR10 (bottom right) as black circles. Each sample was fitted using a "homogeneous core-inhomogeneous shell, spherically capped cylinder model" (red curve). Note: samples GNR1, GNR5 and GNR7 showed an underlying scattering signal from small spheres.

All ten nanorod samples could be fitted well with the core-shell spherically capped cylinder model. The scattering intensity I(q) as a function of scattering vector q for each sample displayed a Guinier region at low scattering vectors $q < 0.1$ Å, where the slope exhibited a q^{-1}-Porod decay, typical for cylindrical particle scattering. This part of the scattering spectrum holds the primary information about the overall size of the particles. Clear form factor oscillations can be seen at higher q-values ($q > 0.1$ Å) and these yielded information about the shape and the internal density distribution. The scattering curves for GNR1, GNR5 and GNR7 showed an additional, overlapping scattering signal from a second type of particle, evident from the deviations of the fit from the signal at several points, particularly at $q = 0.035$ Å. This is attributed to scattering from spherical particles, which were excluded from the fitting process.

The scattering curves provide direct access to the length and width (doubled radius) of the gold nanorods in

solution. The fitted dimensions are displayed in Table 2. All samples are in good agreement with the dimensions measured from the TEM images (compare Fig. 1 and Table 1) to within a few nanometres. Interestingly, the SAXS spectra revealed the presence of a population of spheres in samples GNR1, GNR5 and GNR7 which were not evident in the TEM images. However, significant numbers of gold spheres were seen in TEM images collected from sample GNR3, which were not evident in the SAXS pattern, suggesting that the spheres were over-represented on the dried TEM grid.

Table 2: The dimensions (length, L, and radius, R) from small angle X-ray scattering curves, and standard deviation σ for samples GNR1 to GNR10. The width, W = 2R, while the aspect ratio, AR = L/W.

Sample ID	$\mathbf{L}_{Au}$ **[nm]**	σ_L	$\mathbf{R}_{Au}$ **[nm]**	σ_R	$\mathbf{R}_{CTAB}$	$\mathbf{W}_{Au}$ **[nm]**	**AR**
GNR1	33.5	0.112	3.46	0.261	3.2	6.92	4.84
GNR2	51.4	0.107	5.39	0.16	3.45	10.78	4.77
GNR3	44.5	0.106	4.34	0.113	3.35	8.68	5.13
GNR4	40.9	0.101	3.87	0.113	3.24	7.74	5.28
GNR5	42.0	0.108	4.33	0.14	3.29	8.66	4.85
GNR6	43.7	0.107	3.98	0.11	3.25	7.96	5.49
GNR7	73.2	0.155	6.52	0.176	3.82	13.04	5.61
GNR8	39.9	0.112	4.03	0.132	3.27	8.06	4.95
GNR9	47.6	0.101	4.33	0.113	3.34	8.66	5.50
GNR10	50.5	0.103	3.7	0.115	3.2	7.4	6.82

The dimensions of the nanorods shown in Table 2 are the result of fitting each scattering curve to a spherically capped core-shell cylinder model. The fit yielded an average value of 3.34 nm for the thickness of the CTAB layer, corresponding to a bilayer. This is in agreement with previously published values of 3.2 nm determined by SANS measurements and 3.14 nm by time-resolved SAXS measurements during the growth of the same gold nanorods as used in this work.[3] Shown in the last column of Table 2 are the aspect ratios of the rods, determined by SAXS. These aspect ratios show an overall increase from sample GNR1 to GNR10, which is the same trend already shown for the TEM dimensions in Table 1, and in agreement with the increasing LSPR wavelengths from sample 1 to 10.

3.4 DLS Measurements.

Dynamic light scattering (DLS) measurements estimate the particle size from the Brownian diffusion of the particles in solution. Usually, these samples are highly dilute solutions, which require only a small volume of sample and short acquisition times. However, the sample quality and monodispersity is very important as DLS, much like other scattering methods, always has a bias towards larger particles in suspension.

The intensity autocorrelation functions obtained from each gold nanorod sample for both VV and VH geometries are shown in Figure 3. We have only plotted the curves collected at a scattering angle of 90 °. All autocorrelation functions were fitted with nonlinear least square fits, using equations 7 and 8 for VV and VH geometry respectively. Unlike the procedure adopted in earlier contributions[7], the polydispersity in the rod length was taken into account by integrating over a logarithmic normal distribution of lengths in the fitting routine.

It is readily recognised that all of the intensity autocorrelation functions in VV geometry exhibited two relaxation modes, both of which were dependent on the scattering angle (see Figure S4). The relaxation times of the autocorrelation function in VH geometry on the other hand remained almost unchanged with scattering angle and only displayed one relaxation mode (see Figure S5). This observation appears to be at odds with eqs.7 and 8 since all the exponentials involve a contribution which is proportional to Q^2. However, if $D_r >> D_t Q^2$ only the first term in eq. 7 varies substantially with the scattering angle. Consequently we may safely assume that the slow relaxation mode observed in VV-geometry is related to the translational diffusion of the rods, while the fast mode and the relaxation rates of the signals collected in VH geometry are dominated by the rotational diffusion of the gold rods.

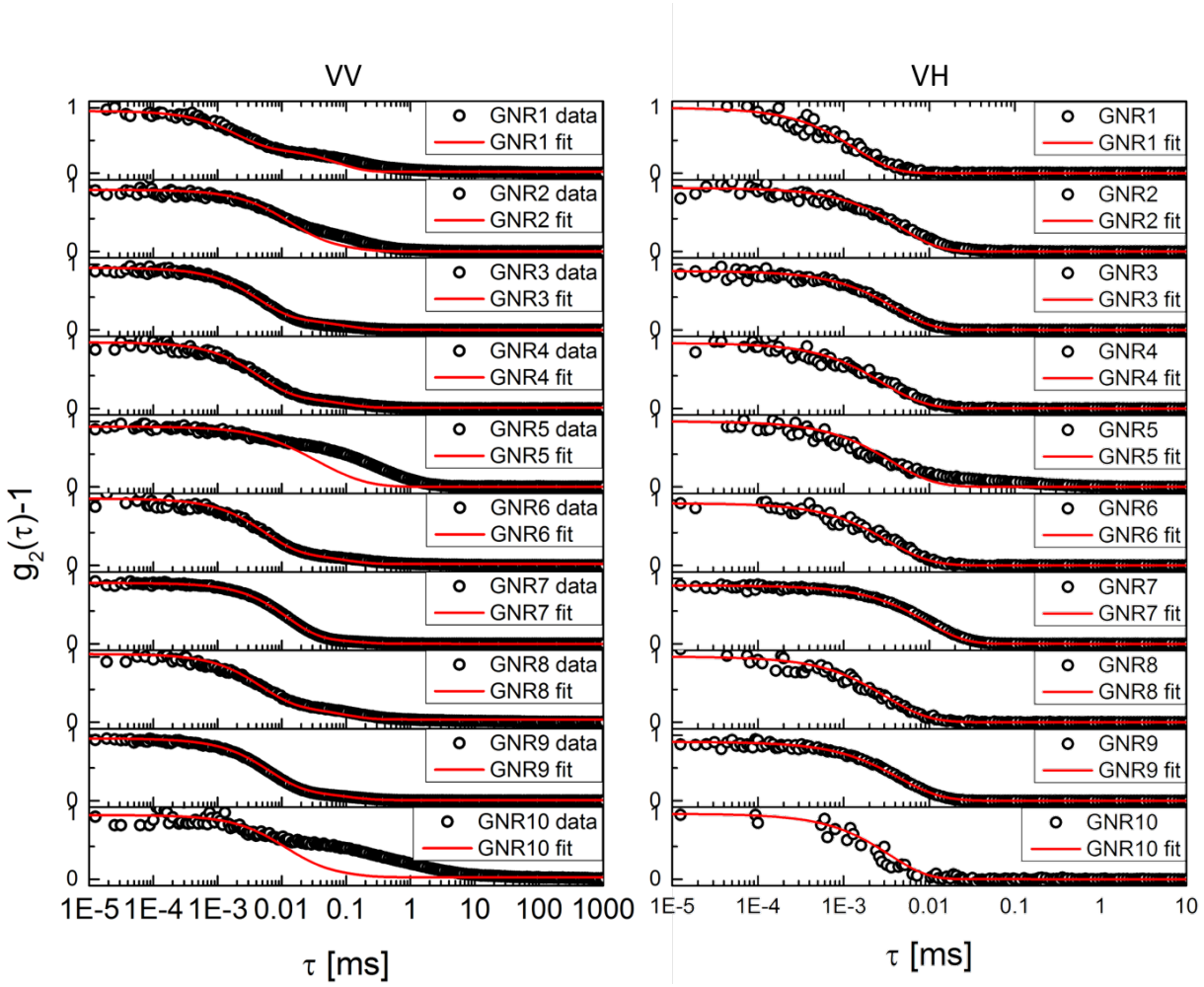

Figure 3: Polarised (VV, left) and depolarised (VH, right) correlation functions of the scattered intensity $g_2(\tau)-1$ as a function of decay time τ for all gold nanorod samples GNR1 to GNR10. The displayed correlation functions were measured at a 90 degree angle. All samples were fitted (red curves) using eqs.7 through 10 as the model functions.

Good agreement was found between the measured intensity auto-correlation functions and the corresponding nonlinear fitting curves according to eqs.7 through 10 for most samples in VV geometry and all the samples in VH geometry. A slight mismatch between VV data and the fit was observed for samples GNR1 and GNR2, which was attributed to slight polydispersity, particularly in thickness of the sample while for samples GNR5 and GNR10 the quality of the acquired data in VV geometry was not good enough for a reasonable fit, as evident from Figure 3. For GNR5 and GNR10, the poorer data quality was also evident in VH geometry; however, due to the absence of the slow relaxation mode, a good fit could still be achieved. The best values of the fitting parameters are listed in Table 3.

Table 3: Length, L, and width, W, and the corresponding standard deviation σ, calculated from DLS measurements with the fitted translational and rotational diffusion coefficients (see Table 4).

Sample ID	$\mathbf{L}_{VV}$ **[nm]**	$\mathbf{W}_{VV}$ **[nm]**	$\sigma_{r,VV}$	$\mathbf{L}_{VH}$ **[nm]**	$\mathbf{W}_{VH}$ **[nm]**	$\sigma_{r,VH}$
GNR1	33	13	0.1	35	13	0.12
GNR2	58	18	0.5	58	17	0.1
GNR3	48	14	0.21	49	20	0.1
GNR4	45	14	0.3	45	14	0.3
GNR5	44	15	0.3	47	16	0.3
GNR6	49	15	0.3	49	14	0.28
GNR7	79	18	0.1	79	18	0.1
GNR8	45	15	0.3	47	14	0.29
GNR9	53	16	0.3	55	15	0.28
GNR10	56	17	0.5	51	16	0.1

The relationship between these geometrical parameters and diffusion constants of colloidal rods has been discussed by Ortega and de la Torre.[28] Utilising their method to correlate the rod diffusion coefficients to the length, L, and width, W, of the measured nanorods, we extracted the translational and rotational diffusion coefficients through eqs.9 and 10 for comparison with the diffusion coefficients obtained by AUC. The resulting values are listed in Table 4. We note that the particle width W as determined by DLS is systematically larger for all GNR than the values from TEM by 6 nm on average. This value corresponds to twice the thickness of the CTAB layer around the rods as found by SAXS. Thus the particles appear bigger in DLS because of the surfactant shell, which is not resolved in TEM.

Table 4: Translational, D_t, and rotational, D_r, diffusion coefficients measured by DLS and calculated using the method of Lang et al. for the 90 degree angle dependent correlation functions shown in Fig. 3 measured in both vertical-vertical (VV) and vertical-horizontal (VH) geometry.[7]

Sample ID	$\mathbf{D}_t$ **(VV)** $[\mathbf{m}^2/\mathbf{s}]$	$\mathbf{D}_r$ **(VV)** $[\mathbf{1}/\mathbf{s}]$	$\mathbf{D}_t$ **(VH)** $[\mathbf{m}^2/\mathbf{s}]$	$\mathbf{D}_r$ **(VH)** $[\mathbf{1}/\mathbf{s}]$
GNR1	2.16E-11	7.65E+04	2.10E-11	6.82E+04
GNR2	1.39E-11	1.78E+04	1.43E-11	1.88E+04
GNR3	1.74E-11	3.33E+04	1.42E-11	2.25E+04
GNR4	1.79E-11	3.81E+04	1.79E-11	3.81E+04
GNR5	1.75E-11	3.74E+04	1.64E-11	3.07E+04
GNR6	1.66E-11	2.99E+04	1.72E-11	3.18E+04
GNR7	1.19E-11	9.16E+03	1.19E-11	9.16E+03
GNR8	1.73E-11	3.57E+04	1.76E-11	3.48E+04
GNR9	1.55E-11	2.40E+04	1.57E-11	2.34E+04
GNR10	1.46E-11	2.02E+04	1.58E-11	2.60E+04

3.5 AUC Measurements.

Analytical ultracentrifugation (AUC) coupled with fast diode acquisition systems allows real time measurement of the rate of sedimentation of nanocrystals[21]. Conversion of the sedimentation coefficients into diffusion coefficients and hence into dimensions, requires an accurate model for the hydrodynamic drag of the particles, f, which itself is strongly shape-dependent. Many models have been derived to approximate f as a function of dimensions for rod-like particles over the past few decades.[28–35] There is general agreement between these models although there are subtle differences. Mansfield[34] and Aragon[35] employed a spherically capped cylinder description, also known as a blunt cylinder, where the ends of the rod were imagined as symmetrical hemispheres. Thus, the calculated values for f were smaller than the ones for flat-ended cylinders[28], core-shell rigid rods[15] or elongated ellipsoids[36]. This can explain discrepancies in various data sets[7,11].

As discussed above, the diffusion coefficient, D, is a function of the size and shape of a nanocrystal. Using the numerical interpolations proposed by Aragon and Flamik[35], we extracted values for L and W from the sedimentation data. The CTAB layer also affecs the sedimentation rate and we assumed the presence of a 3.2nm CTAB layer in order to determine the gold core dimensions. A spectral model provided by Near[37] may be used to further constrain the L and W dimensions of the GNRs based on the LSPR peak position. However, the

function provided by Near et al. serves as a generalisation of the DDSCAT methodology, which can therefore be applied to cylinders of various size and aspect ratio. By combining the spectral model and sedimentation behavior, as modeled by the Svedberg equation, the values of L and W for the particles may then be determined. The value for D_t may then also be computed.

In Figure 4, we show the sedimentation distributions obtained in water for samples GNR1-10. Generally the smaller gold rods ceded narrower size distributions. Importantly, there was little evidence for significant concentrations of spherical gold nanocrystals. In Table 5, we present the extracted values for the length and width and diffusion coefficient of the rods. Note these have been analysed after accounting for the CTAB layer. The raw data is tabulated in Table S4.

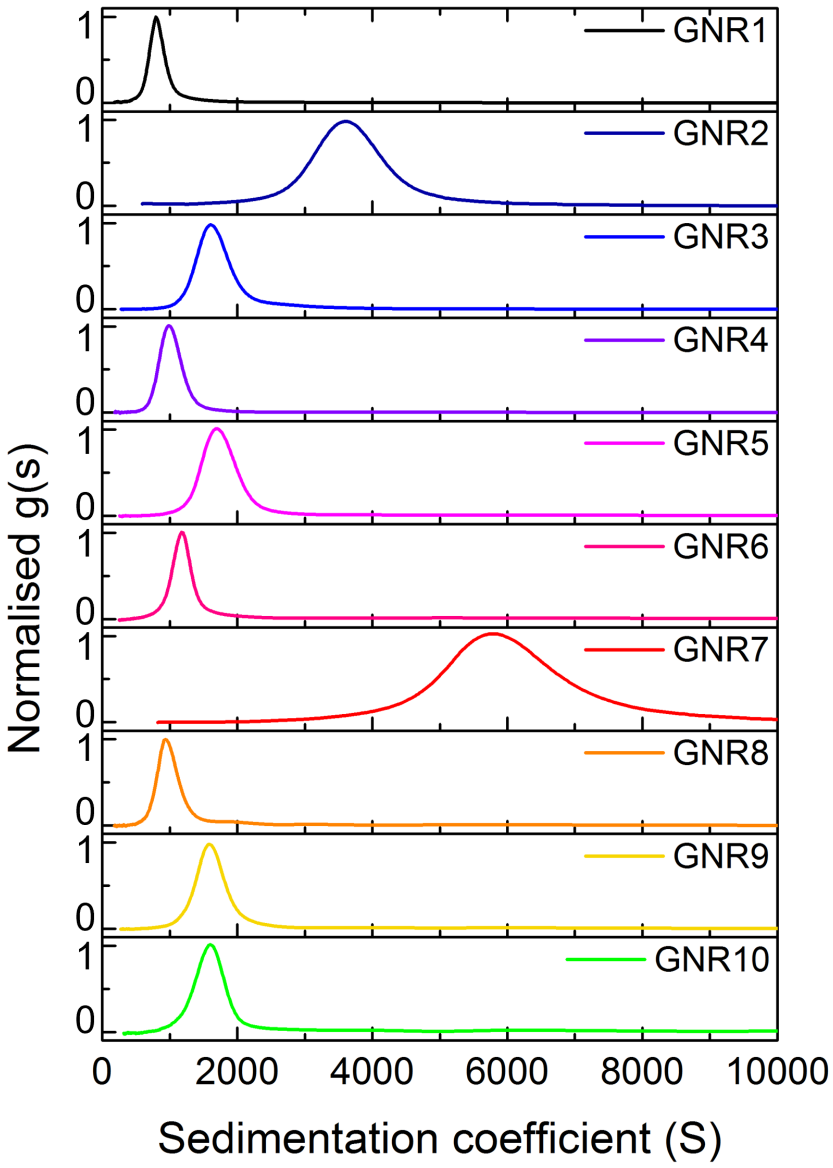

Figure 4: Sedimentation coefficient distributions of the synthesised gold nanorod samples GNR1 (top) to GNR10 (bottom) determined by AUC in water. See Table 5 for the derived dimensions of the rods in each sample.

Table 5: The Lengths, L, and widths, W of the gold rods determined from AUC measurements (i.e. the sedimentation coefficients (S)) assuming a constant CTAB shell thickness of 3.2 nm. The collected data also yield values for the LSPR peak wavelength (nm), and the translational rod diffusion coefficients (D_t).

Sample ID	**L_{Au} [nm]**	**W_{Au} [nm]**	**D [m^2/s]**	**S [sved]**
GNR1	25.2	6.9	2.06E-11	803.20
GNR2	49.2	13.4	1.26E-11	3620.7
GNR3	37.4	9.1	1.61E-11	1622.64
GNR4	32.1	7.2	1.84E-11	993.7
GNR5	38.0	9.3	1.58E-11	1711.3
GNR6	37.2	7.5	1.69E-11	1171
GNR7	67.9	16.1	1.02E-11	5850.44
GNR8	34.3	6.8	1.80E-11	960.40
GNR9	43.1	8.5	1.53E-11	1591.2
GNR10	44.0	8.5	1.51E-11	1587.4

3.6 Predictions of the SPR Wavelength

The above sections present results from four different techniques used to determine the dimensions of gold nanorods. To decide which of these methods cedes the most accurate values is vexing and subjective. Each has its own advantages and disadvantages. Given the importance of the optical properties of these particles, our approach is to examine how well the extracted values can predict the surface plasmon resonance of the same samples. The extinction spectra of the ten gold nanorod samples are shown in Figure 5. Extinction spectra of the synthesised gold nanorod samples GNR1 (top) to GNR10 (bottom) were collected in a wavelength range between 400 and 1050 nm. The spectra were measured with an Agilent HP 8453 and a Cary 5000 spectrometer. The spectra evinced two clear peaks, with one near 510 nm due to the transverse surface plasmon mode and a much more intense mode at longer wavelengths ranging between 760nm and 970 nm due to the longitudinal surface plasmon resonance (LSPR). We focus on the longitudinal mode. While the exact peak position is also influenced by polydispersity, the rods investigated here are reasonably monodisperse. It is therefore useful to assess whether the dimensions gleaned from the sizing experiments are able to predict the peak wavelength. We do not attempt to reproduce the SPR lineshape since the broadening is affected by a large number of parameters.

Even to predict the peak wavelength, we must a priori assume a geometry and we use a spherically capped cylinder, which is consistent with the morphology from TEM and the SAXS fitting. Extensive previous work has also shown that this geometry is more accurate than the simpler ellipsoidal morphology used in earlier work. We have inputted the mean lengths and widths from TEM and SAXS into COMSOL and compare the simulated plasmon peak for the longitudinal resonances to the ensemble spectrum. The results are presented in Figure 5 and listed in Table 6.

Table 6: Comparison of the LSPR peak wavelengths for the gold nanorod samples GNR1-10 determined experimentally and using COMSOL with the mean values of the length and width from TEM and SAXS Measurements. Also shown are the LSPR peak wavelengths measured in the AUC after separation from spheres.

Sample ID	**$LSPR_{Abs}$ [nm]**	**$LSPR_{TEM}$ [nm]**	**$LSPR_{SAXS}$ [nm]**	**$LSPR_{AUC}$ [nm]**
GNR1	760	785	895	765
GNR2	800	775	895	772
GNR3	810	835	930	820
GNR4	860	870	945	859
GNR5	860	815	900	815
GNR6	900	935	965	915
GNR7	880	910	995	840
GNR8	910	905	905	918
GNR9	920	935	960	925
GNR10	970	935	1110	943

Overall, we see that TEM yields the most accurate predictions for the ensemble peak position. Polydispersity is not included here, i.e. only the mean length and mean widths were used to calculate the spectra. This results in artificially narrow resonances. In virtually all cases, SAXS yields values slightly red-shifted from those of TEM. Comparing the values in Tables 1 and 2, we see that the difference arises primarily from the under-estimation

of the rod width in SAXS, which results in an over-estimation of the aspect ratio. The rod lengths are quite consistent between the two methods. This Table also includes values from AUC but note that these are simply the recorded peak positions in the AUC after centrifugation and not simulated data.

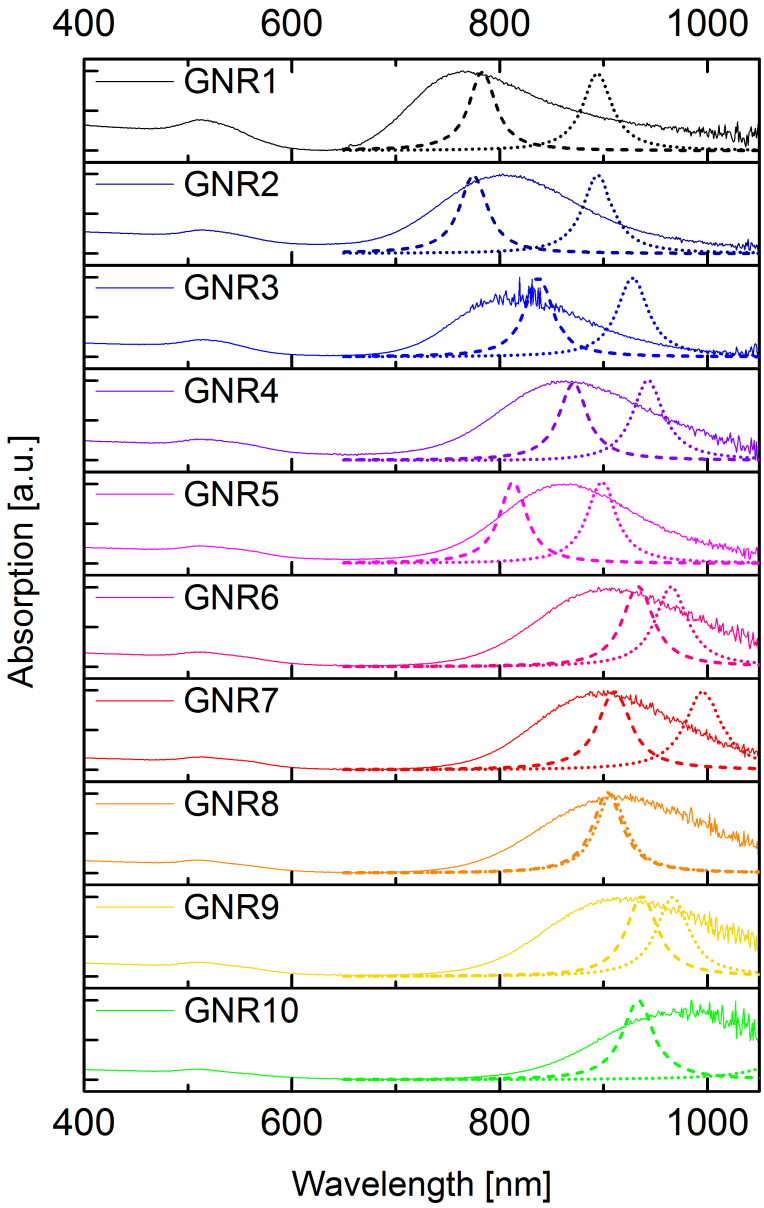

Figure 5: Experimental spectra of the gold nanorod samples GNR1-10 and COMSOL simulations. Experimental data (solid lines). TEM = dashed lines. SAXS = dotted lines. A spherically capped cylinder was used with dimensions from Table 1 and Table 2. The CTAB layer was not included in the COMSOL simulation and would result in a small red-shift of the predicted spectra. Refractive index of water = 1.33.

3.7 Comparing the Methods

The accurate determination of particle dimensions at the nanoscale is an essential step towards a better understanding of plasmonics. In general, all four of the analytical methods chosen share the advantages that they are: non-destructive, require only small sample volumes and need relatively short acquisition times. A more detailed list of advantages and disadvantages of each method is provided in Table S2.

Using the above described methods on a set of 10 uniform gold nanorod samples, the following three main points can be made:

i) Spherically capped cylinders deliver the best description of the gold nanorod shape and size, compared to ellipsoids or spheres.

ii) The solution based methods yield better fits when the CTAB shell is included in the fitting process. Calculated graphs comparing DLS in the presence and absence of the CTAB shell can be found in the SI.

iii) A combination of methods is required to obtain the best, all-encompassing sample information. No one method is able to deliver the full picture of all sample attributes.

3.7.1 Longitudinal surface plasmon resonance

Individual researchers may argue for or against the accuracy or precision of the different methods used here. Ultimately, the ability of the techniques to cede accurate values of some size-dependent rod property provides a useful test of the analytical procedures. To this end, we have calculated the longitudinal surface plasmon resonance (LSPR) peak wavelength predicted by the TEM and SAXS using COMSOL and compared them to the experimentally determined spectral peak wavelengths (see Table 6). These two methods gave the closest match to COMSOL. See Figures S6-S8 for graphical results for all of the four techniques.

What is clear is that only TEM consistently predicts peak wavelengths close to the experimentally observed ensemble values. Table 6 also presents the peak positions observed for the ensembles in AUC. Since AUC is a size distribution and exclusion method, the rods can be separated from the spheres and the in situ extinction spectrum recorded of the rod fraction alone. The plasmon peak measured by AUC is in very good agreement with the experimental LSPR peaks from the absorption spectra of the rod samples. This confirms simply that the AUC did not damage the samples or induce coagulation even at high centrifugation speeds. It also shows that the SPR peak wavelegth is not strongly affected by the small populations of spheres present. We also see that AUC is able to estimate size distributions even if the absolute values are less accurate than TEM or SAXS.Samples with broad distributions in AUC correspond to those with broader absorption spectra.

As is evident from Figures S7 and S8, the length and width are both in very good agreement across all methods. As expected, DLS yields consistently larger values for both length and width across all samples, due to the fact it measures the solution state of the particle, including the CTAB shell and any Stern-layer-bound water layer, and will generally be slightly larger than the core + shell seen in SAXS (for a discussion see Eitel et al. [6]). There is better agreement between TEM, SAXS and AUC values when a CTAB layer of around 3 nm radius is assumed.

3.7.2 CTAB shell Thickness

The advantage of SAXS in particular is that it probes both the particle structure and the surrounding surfactant layer. In the case of DLS and AUC, the shell thickness is inferred from the combination of diffusion data and the TEM rod dimensions. The results for the CTAB shell thickness for each of the three methods for samples GNR 1 to 10, as well as the calculated average values are shown in Table 7. All three methods yield consistent values for the CTAB shell thickness and these are more or less independent of the rod dimensions, with an average CTAB layer thickness between 3 nm and 3.3 nm, which is in good agreement with previous studies. [3,7] It is important to note, however, that DLS cannot yield values for the surfactant shell thicknesses without independent values for the particle core dimensions obtained using another technique. Hence, in this case we calculated it by taking the DLS value, subtracting the TEM or SAXS values to get a value corresponding to twice the shell thickness, and then halving it and averaging the TEM and SAXS values to generate the value T(DLS) shown in the table.

These values are very consistent across the three methods shown and provide strong statistical evidence that CTAB forms a bilayer on the gold nanorod surface. We note there is excellent agreement with the values obtained by Liz-Marzán and colleagues using SANS data [38]. While the mean values obtained here are in strong agreement, the standard deviations increase from SAXS to DLS to AUC.

4 Conclusions

We have presented a systematic study of the four most common methods used to size nanocrystals. Gold rods are an ideal probe since they: present strong X-ray contrast, exhibit strong electron scattering, possess large refractive index contrast and have an extremely high density contrast, making them ideal probes for such a

Table 7: CTAB shell size (thickness) from SAXS, DLS (calculated with TEM and SAXS values as comparison) and AUC. Mean values and corresponding standard deviations are shown in the last row.

Sample ID	$\mathbf{T}_{SAXS}$ **[nm]**	$\mathbf{T}_{DLS}$ **[nm]**	$\mathbf{T}_{AUC}$ **[nm]**
GNR1	3.2	2.87	2.46
GNR2	3.45	2.67	4.62
GNR3	3.35	3.22	2.95
GNR4	3.24	3.13	2.57
GNR5	3.29	2.72	2.95
GNR6	3.25	3.02	2.67
GNR7	3.82	2.96	5.74
GNR8	3.27	3.10	2.63
GNR9	3.34	3.11	2.93
GNR10	3.2	3.57	2.94
average (+s.d.)	3.34 ± 0.18	3.02 ± 0.26	3.22 ± 1.07

study. Furthermore, shape control of gold nanocrystals is well advanced. From Table S3 and Figure S6, we see that all four methods provide reasonable values for the rod dimensions. Prediction of the SPR resonance peak however emphasizes small errors in the aspect ratio, which in turn amplifies any errors in the precise determination of the rod width. Overall, TEM still offers the most consistent method for determination of both size and aspect ratio, although this is possibly only true for close to monodisperse samples. X-ray scattering provides a useful alternative that allows accuracy within 10% of TEM for most lengthscales and can give information in dynamic situations such as realtime monitoring of nanocrystal growth, shape changes or dissolution.

AUC and DLS are both relatively simple methods in terms of sample preparation but because they yield the overall hydrodynamic diameter, the core size can only be extracted if ligand and coating information can be garnered though independent means. Both AUC and TEM can provide estimates of the fractions of particles with different morphologies in the samples but it is evident this requires careful pre-calibration of each system under investigation.

Although AUC was originally developed to size gold particles, it is also clear from the results here that the ligand shell must be accounted for when analysing the sedimentation profiles in order to extract the correct core sizes. Both the ligand shell thickness (out to the shear plane), as well as the ligand shell density must be known with some precision since the ligand shell occupies a significant volume of any nanocrystal. It is unclear at present how this can be achieved.

5 Supporting Information

The Supporting iInformation includes a detailed description of the used COMSOL simulations, DLS raw data, a tabular comparison including advantages and disadvantages of the used characterisation techniques, data summary tables to present all raw data used in this manuscript, as well as fitted DLS correlation functions to show the difference between inclusion and exclusion of shell thickness in particle size in addition to examples of angle dependent DLS data. We also included visualisation plots of GNR size parameters and comparisons between different techniques to show correlations.

6 Acknowledgements

The authors thank the ARC for support through CE170100026. SS acknowledges the support of a PhD stipend through the Melbourne-Bayreuth joint PhD program and the Bayreuth-Melbourne colloid polymer network. SAXS data was collected at the SAXS/WAXS beamline of the Australian Synchrotron, ANSTO as part of grant number M13158.

References

[1] Oshikiri, T.; Ueno, K.; Misawa, H. Selective Dinitrogen Conversion to Ammonia Using Water and Visible Light through Plasmon-induced Charge Separation. *Angewandte Chemie International Edition* **2016**, *55*, 3942–3946.

[2] Nishijima, Y.; Ueno, K.; Yokota, Y.; Murakoshi, K.; Misawa, H. Plasmon-Assisted Photocurrent Generation from Visible to Near-Infrared Wavelength Using a Au-Nanorods/TiO $_2$ Electrode. *The Journal of Physical Chemistry Letters* **2010**, *1*, 2031–2036.

[3] Seibt, S.; Zhang, H.; Mudie, S.; Förster, S.; Mulvaney, P. Growth of Gold Nanorods: A SAXS Study. *The Journal of Physical Chemistry C* **2021**, *125*, 19947–19960.

[4] Goldstein, J. I.; Newbury, D. E.; Michael, J. R.; Ritchie, N. W.; Scott, J. H. J.; Joy, D. C. *Scanning Electron Microscopy and X-Ray Microanalysis*; Springer New York: New York, NY, 2018; pp 1–63.

[5] Schöpe, H. J.; Marnette, O.; van Megen, W.; Bryant, G. Preparation and Characterization of Particles with Small Differences in Polydispersity. *Langmuir* **2007**, *23*, 11534–11539.

[6] Eitel, K.; Bryant, G.; Schöpe, H. J. A Hitchhiker's Guide to Particle Sizing Techniques. *Langmuir* **2020**, *36*, 10307–10320.

[7] Rodríguez-Fernández, J.; PérezJuste, J.; LizMarzán, L. M.; Lang, P. R. Dynamic Light Scattering of Short Au Rods with Low Aspect Ratios. *The Journal of Physical Chemistry C* **2007**, *111*, 5020–5025.

[8] Reddy, N. K.; Pérez-Juste, J.; Pastoriza-Santos, I.; Lang, P. R.; Dhont, J. K. G.; Liz-Marzán, L. M.; Vermant, J. Flow Dichroism as a Reliable Method to Measure the Hydrodynamic Aspect Ratio of Gold Nanoparticles. *ACS Nano* **2011**, *5*, 4935–4944.

[9] Sutherland, W. A dynamical theory of diffusion for non-electrolytes and the molecular mass of albumin. *The London, Edinburgh, and Dublin Philosophical Magazine and Journal of Science* **1905**, *9*, 781–785.

[10] Einstein, A. Über die von der molekularkinetischen Theorie der Wärme geforderte Bewegung von in ruhenden Flüssigkeiten suspendierten Teilchen. *Annalen der Physik* **1905**, *322*, 549–560.

[11] Glidden, M.; Muschol, M. Characterizing Gold Nanorods in Solution Using Depolarized Dynamic Light Scattering. *The Journal of Physical Chemistry C* **2012**, *116*, 8128–8137.

[12] Levin, A. D.; Shmytkova, E. A.; Khlebtsov, B. N. Multipolarization Dynamic Light Scattering of Nonspherical Nanoparticles in Solution. *The Journal of Physical Chemistry C* **2017**, *121*, 3070–3077.

[13] Feller, D.; Otten, M.; Hildebrandt, M.; Krüsmann, M.; Bryant, G.; Karg, M. Translational and rotational diffusion coefficients of gold nanorods functionalized with a high molecular weight, thermoresponsive ligand: a depolarized dynamic light scattering study. *Soft Matter* **2021**, *17*, 4019–4026.

[14] Siebrands, T.; Giersig, M.; Mulvaney, P.; Fischer, C. H. Steric exclusion chromatography of nanometer-sized gold particles. *Langmuir* **1993**, *9*, 2297–2300.

[15] Silvera Batista, C. A.; Zheng, M.; Khripin, C. Y.; Tu, X.; Fagan, J. A. Rod Hydrodynamics and Length Distributions of Single-Wall Carbon Nanotubes Using Analytical Ultracentrifugation. *Langmuir* **2014**, *30*, 4895–4904.

[16] Thajudeen, T.; Walter, J.; Uttinger, M.; Peukert, W. A Comprehensive Brownian Dynamics-Based Forward Model for Analytical (Ultra)Centrifugation. *Particle & Particle Systems Characterization* **2017**, *34*, 1600229.

[17] Fagan, J. A.; Zheng, M.; Rastogi, V.; Simpson, J. R.; Khripin, C. Y.; Silvera Batista, C. A.; Hight Walker, A. R. Analyzing Surfactant Structures on Length and Chirality Resolved (6,5) Single-Wall Carbon Nanotubes by Analytical Ultracentrifugation. *ACS Nano* **2013**, *7*, 3373–3387.

[18] Wawra, S. E.; Pflug, L.; Thajudeen, T.; Kryschi, C.; Stingl, M.; Peukert, W. Determination of the two-dimensional distributions of gold nanorods by multiwavelength analytical ultracentrifugation. *Nature Communications* **2018**, *9*, 4898.

[19] Cardenas Lopez, P.; Uttinger, M. J.; Traoré, N. E.; Khan, H. A.; Drobek, D.; Apeleo Zubiri, B.; Spiecker, E.; Pflug, L.; Peukert, W.; Walter, J. Multidimensional characterization of noble metal alloy nanoparticles by multiwavelength analytical ultracentrifugation. *Nanoscale* **2022**, *14*, 12928–12939.

[20] Frank, U.; Drobek, D.; Sánchez-Iglesias, A.; Wawra, S. E.; Nees, N.; Walter, J.; Pflug, L.; Apeleo Zubiri, B.; Spiecker, E. et al. Determination of 2D Particle Size Distributions in Plasmonic Nanoparticle Colloids via Analytical Ultracentrifugation: Application to Gold Bipyramids. *ACS Nano* **2023**, *17*, 5785–5798.

[21] Planken, K. L.; Cölfen, H. Analytical ultracentrifugation of colloids. *Nanoscale* **2010**, *2*, 1849.

[22] Pearson, J.; Cölfen, H. LED based near infrared spectral acquisition for multiwavelength analytical ultracentrifugation: A case study with gold nanoparticles. *Analytica Chimica Acta* **2018**, *1043*, 72–80.

[23] Polte, J.; Ahner, T. T.; Delissen, F.; Sokolov, S.; Emmerling, F.; Thünemann, A. F.; Kraehnert, R. Mechanism of Gold Nanoparticle Formation in the Classical Citrate Synthesis Method Derived from Coupled In Situ XANES and SAXS Evaluation. *Journal of the American Chemical Society* **2010**, *132*, 1296–1301.

[24] Polte, J.; Erler, R.; Thünemann, A. F.; Sokolov, S.; Ahner, T. T.; Rademann, K.; Emmerling, F.; Kraehnert, R. Nucleation and Growth of Gold Nanoparticles Studied *via in situ* Small Angle X-ray Scattering at Millisecond Time Resolution. *ACS Nano* **2010**, *4*, 1076–1082.

[25] Förster, S.; Apostol, L.; Bras, W. Scatter : software for the analysis of nano- and mesoscale small-angle scattering. *Journal of Applied Crystallography* **2010**, *43*, 639–646.

[26] Cusack, S.; Miller, A.; Krijgsman, P.; Mellema, J. An investigation of the structure of Alfalfa mosaic virus by small-angle neutron scattering. *Journal of Molecular Biology* **1981**, *145*, 525–543.

[27] Nixon-Luke, R.; Bryant, G. A Depolarized Dynamic Light Scattering Method to Calculate Translational and Rotational Diffusion Coefficients of Nanorods. *Particle & Particle Systems Characterization* **2019**, *36*, 1800388.

[28] Ortega, A.; Garcıa de la Torre, J. Hydrodynamic properties of rodlike and disklike particles in dilute solution. *The Journal of Chemical Physics* **2003**, *119*, 9914–9919.

[29] Norisuye, T.; Motowoka, M.; Fujita, H. Wormlike Chains Near the Rod Limit: Translational Friction Coefficient. *Macromolecules* **1979**, *12*, 320–323.

[30] Batchelor, G. K. The stress system in a suspension of force-free particles. *Journal of Fluid Mechanics* **1970**, *41*, 545–570.

[31] Tirado, M. M.; de la Torre, J. G. Translational friction coefficients of rigid, symmetric top macromolecules. Application to circular cylinders. *The Journal of Chemical Physics* **1979**, *71*, 2581–2587.

[32] Tirado, M. M.; de la Torre, J. G. Rotational dynamics of rigid, symmetric top macromolecules. Application to circular cylinders. *The Journal of Chemical Physics* **1980**, *73*, 1986–1993.

[33] Tirado, M. M.; Martínez, C. L.; de la Torre, J. G. Comparison of theories for the translational and rotational diffusion coefficients of rod-like macromolecules. Application to short DNA fragments. *The Journal of Chemical Physics* **1984**, *81*, 2047–2052.

[34] Mansfield, E. D.; Reinhardt, E. International Institutions and the Volatility of International Trade. *International Organization* **2008**, *62*, 621–652.

[35] Aragon, S. R.; Flamik, D. High Precision Transport Properties of Cylinders by the Boundary Element Method. *Macromolecules* **2009**, *42*, 6290–6299.

[36] Martchenko, I.; Dietsch, H.; Moitzi, C.; Schurtenberger, P. Hydrodynamic Properties of Magnetic Nanoparticles with Tunable Shape Anisotropy: Prediction and Experimental Verification. *The Journal of Physical Chemistry B* **2011**, *115*, 14838–14845.

[37] Near, R. D.; Hayden, S. C.; El-Sayed, M. A. Thin to Thick, Short to Long: Spectral Properties of Gold Nanorods by Theoretical Modeling. *The Journal of Physical Chemistry C* **2013**, *117*, 18653–18656.

[38] Mosquera, J.; Wang, D.; Bals, S.; Liz-Marzán, L. M. Surfactant Layers on Gold Nanorods. *Accounts of Chemical Research* **2023**, *56*, 1204–1212.

Supporting Information

Size, Diffusion and Sedimentation of Gold Nanorods

Susanne Seibt[a,b,c,*], Joseph Pearson[d], Reece Nixon-Luke[e], Heyou Zhang[b], Peter R. Lang[f], Gary Bryant[e], Helmut Cölfen[d], Paul Mulvaney[b]

[a] *SAXS / WAXS Beamline, Australian Synchrotron, ANSTO, 800 Blackburn Road, VIC-3168 Clayton, Australia.*
[b] *ARC Centre of Excellence in Exciton Science, School of Chemistry, The University of Melbourne, Parkville, VIC 3010, Australia.*
[c] *Physical Chemistry I, University of Bayreuth, Universitätsstraße 30, 95448 Bayreuth, Germany*
[d] *Physical Chemistry, University of Konstanz, Universitätsstraße 10, 78457 Konstanz, Germany.*
[e] *School of Science, RMIT University, VIC-3038 Melbourne, Australia.*
[f] *Institute of Biomacromolecular Systems and Processes, Research Centre Jülich, 52425 Jülich, Germany.*

1 Appendix / SI

1.1 COMSOL Simulations:

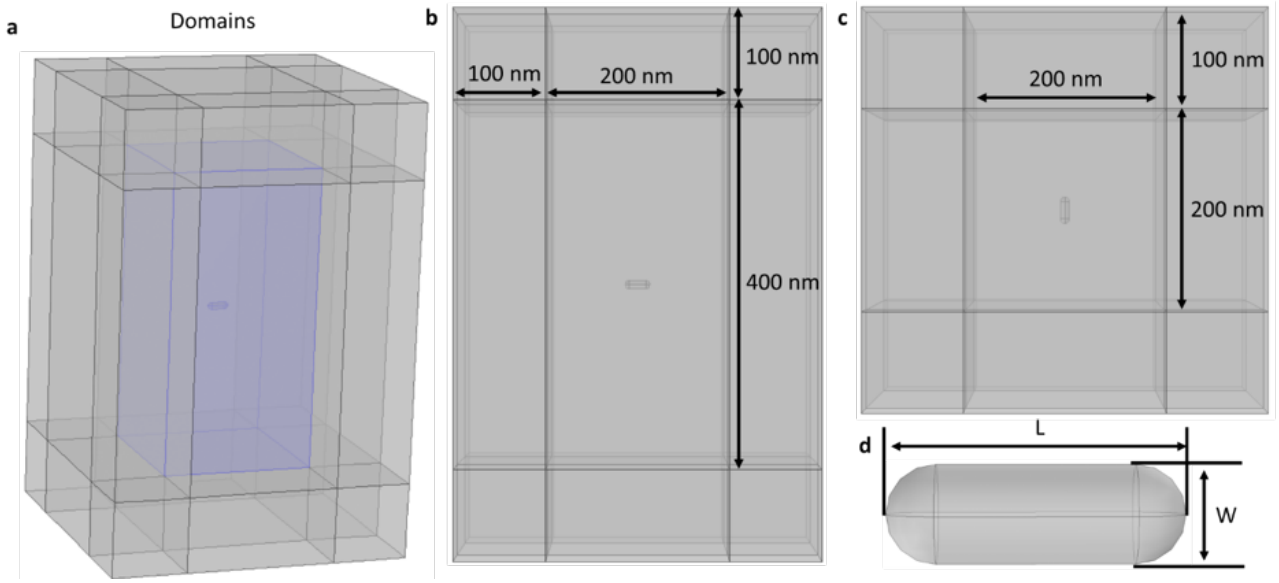

Figure S1: Domain and geometry demonstration used in COMSOL Multiphysics simulation. (a) Two domains are used in the model. Physical domain (blue body) contains a single gold nanorod and its surrounding environment. Outside this is a perfectly matched layer (PML) domain (grey outer layer). (b) and (c): side and top views of the model showing the dimensions used. (d) geometry of the spherically capped cylindrical gold nanorod built in the model.

1.1.1 Parameter details and boundary conditions.

All simulations are based on the finite element method by solving Maxwell's equations:

$$\nabla \times \mu_r^{-1} \left(\nabla \times \overrightarrow{E} \right) - k_0^2 \left(\epsilon_r - \frac{j\sigma}{\omega \epsilon_0} \right) \overrightarrow{E} = 0 \tag{S1}$$

$$\nabla \times \left(\nabla \times \overrightarrow{E} \right) - k_0^2 \epsilon_r \overrightarrow{E} = 0 \tag{S2}$$

The simulations were carried out in two steps. The first step involves only the physical domain to generate the illumination for particle absorption and scattering. The range of the spectrum was simulated from 500 nm to 1100 nm with 5 nm steps. The refractive index of the surrounding environment was set as 1.33 and the refractive index of the gold nanoparticle was taken from Olmon et al.[1] The top face boundary of the physical domain was set to be port 1 (excitation direction), where a polarized electric field (parallel to the gold nanorod longitudinal axis) with a normalized amplitude of 1V/m was generated as the illumination source. This electric field propagated through the physical domain and terminated at the bottom face boundary of the physical domain, which was set as port 2. The remaining four sides were set to have periodic boundary conditions in order to generate evenly distributed electric fields across the entire physical domain. The resulting three components of the electric field in the x, y, and z directions (emw.Ex, emw.Ey and emw.Ez) were further used for the second step.

The second simulation step involves both the physical domain and the PML domain. The "formula option" for this simulation step was chosen for the scattered field, which solves the perturbation to the total field caused by the scatterer (gold nanorod) including scattered intensity (Poynting) and power loss density. An incident wave (background electric field) was used for triggering the extinction processes by the nanorod. This incident wave was defined in terms of the three components in the x, y and z directions by using the resulting electric field from the first step (emw.Ex, emw.Ey and emw.Ez). The refractive index of the PML was also set as

1.33. After simulation, the time-averaged Poynting vector components of the scattered field were calculated (emw2.relPoavx, emw2.relPoavy, and emw2.relPoavz) as well as the total power dissipation density (emw2.Qh). These two parameters were further used to calculate the scattering cross section and the absorption cross-section by integrating over the nanorod surface and volume respectively. For the absorption cross-section results shown in this manuscript, the resulting total power dissipation density (emw2. Qh) for a given size gold nanorod was integrated over the volume of the particle and normalized by the intensity of incident field. The final result was plotted as a function of input wavelength as the absorption cross section spectrum.

1.2 Dynamic Light Scattering:

Here we present the raw data from DLS measurements that were carried out using depolarised light scattering.In general better fits were obtained when calculated curves included the CTAB shell (blue) for both VV and VH geometry.

Table S1: Length, L, width, W and CTAB shell thickness as determined from AUC measurements. The collected data also yield information about the translational diffusion coefficients (D_t) and sedimentation coefficients (S).

Sample ID	$\mathbf{L}_{Au}$ **[nm]**	$\mathbf{W}_{Au}$ **[nm]**	$\mathbf{T}_{CTAB}$ **[nm]**	$\mathbf{D}_t$ **[m^2/s]**	**S [sved]**
GNR1	27.0	7.4	2.5	1.69E-11	803
GNR2	56.1	15.4	4.6	8.45E-12	3621
GNR3	41.0	1.0	3.0	1.21E-11	1623
GNR4	34.3	7.7	2.6	1.49E-11	994
GNR5	41.2	10.1	3.0	1.24E-11	1711
GNR6	39.9	8.0	2.7	1.37E-11	1171
GNR7	72.3	17.2	5.7	8.51E-12	5850
GNR8	37.9	7.6	2.6	1.28E-11	960
GNR9	46.6	9.3	2.9	1.20E-11	1591
GNR10	47.6	9.2	2.9	1.19E-11	1587

1.3 Comparing the Different Techniques

Here we present some of the plots comparing the lengths, widths and aspect ratios as determined by the 4 techniques against one another. Of course the fundamental problem is to establish which technique provides the baseline reference data. We use TEM as the reference and plot the determined mean lengths and mean widths vs the mean values from TEM. It is evident that the three other techniques do a good job predicting the length but there is enormous discrepancies for the nanorod widths. Since the aspect ratio is Length/Width, this leads to large differences in the predicted mean aspect ratios. This results in extensive scatter in the predictions of the SPR peak wavelength, as evident in the final plot, even for TEM.

Table S2 presents a summary of the basic pros and cons of each method used in the paper.

Table S2: Pros and cons of all methods in comparison

Technique	**NR state**	**Parameters**	**Advantages**	**Limitations**
UV-Vis	In solution	Optical information	Rapid and cheap, provides information on general growth and optical properties.	No direct information of particle morphology.
TEM	High vacuum	Size, size distribution and shape	Particle morphology at sub-nm resolution, information on internal structure of the particles.	High energy beams, small part of sample, no surfactant shell information. High costs
SAXS	Dry and in solution	Size, size distribution and shape	High sensitivity, compatible for all sample environments, direct information of sample morphology in solution.	Previous knowledge of rough particle morphology is required for fitting of data.
DLS	In solution	Size (hydrodynamic radius) and size distribution, diffusion coefficient	Rapid, provides information of nanoparticle behaviour in solution, can give information about particle morphology.	Highly biased towards larger particles in suspension, inferring information of particle shape and size needs fitting models.
AUC	In solution	Size (hydrodynamic radius) and distribution, mass and density, diffusion and sedimentation coefficient, optical information	High sensitivity, compatible with multimodal populations.	High-cost equipment, needs expertise, dependence on fitting model.

In Table S3 we summarise the final sets of data for the rod length and width using all 4 methods. All the values for length L and width W of samples GNR 1 to 10 are shown in Table S3 after allowing for the CTAB shell and after averaging over different orientations, for example in the case of diffusion coefficients.

Table S3: The lengths and widths of the gold nanorod (core) samples as determined by TEM, SAXS, DLS (average of VV and VH) and AUC.

Sample ID	$\mathbf{L}_{TEM}$ **[nm]**	$\mathbf{L}_{SAXS}$ **[nm]**	$\mathbf{L}_{DLS}$ **[nm]**	$\mathbf{L}_{AUC}$ **[nm]**	$\mathbf{W}_{TEM}$ **[nm]**	$\mathbf{W}_{SAXS}$ **[nm]**	$\mathbf{W}_{DLS}$ **[nm]**	$\mathbf{W}_{AUC}$ **[nm]**
GNR1	28.39	33.5	34	27.0	7.47	6.92	13	7.38
GNR2	52.80	51.4	58	56.1	14.68	10.78	17.5	15.37
GNR3	42.17	44.5	48.5	41.03	9.90	8.68	17	9.97
GNR4	36.40	40.9	45	34.4	7.90	7.74	14	7.67
GNR5	42.75	42.0	45.5	41.2	10.63	8.66	15.5	10.12
GNR6	42.93	43.7	49	39.9	8.28	7.96	14.5	8.04
GNR7	71.98	73.2	79	72.29	17.05	13.04	18	17.20
GNR8	40.09	39.9	46	37.85	8.16	8.06	14.5	7.58
GNR9	48.54	47.6	54	46.6	9.35	8.66	15.5	9.25
GNR10	50.27	50.5	53.5	47.6	9.77	6.82	16.5	9.17

1.4 Diffusion coefficient

DLS and AUC both yield diffusion coefficients, D, and/or sedimentation coefficients, S. The diffusion coefficient from AUC was not measured directly, as the analysis method used in this study ignores diffusion, however it can be calculated from the resulting size parameters of the rod samples. As gold nanorods are anisotropic particles, the measured diffusion coefficient is due to both translational motion which yields D_t and rotational tumbling, which gives rise to rotational diffusion, characterised by D_r. The resulting diffusion coefficients from DLS and AUC for all samples are shown in Table S4.

Table S4: Diffusion coefficient comparison from DLS (average D_t and D_r) and AUC.

Sample ID	**D_t (DLS) [m^2/s]**	**D_r (DLS) [1/s]**	**D_t (AUC) [m^2/s]**
GNR1	2.13E-11	7.24E+04	1.67E-11
GNR2	1.41E-11	1.83E+04	8.45E-12
GNR3	1.61E-11	2.79E+04	1.21E-11
GNR4	1.79E-11	3.81E+04	1.49E-11
GNR5	1.69E-11	3.40E+04	1.24E-11
GNR6	1.69E-11	3.09E+04	1.37E-11
GNR7	1.19E-11	9.16E+03	8.51E-12
GNR8	1.74E-11	3.52E+04	1.28E-11
GNR9	1.56E-11	2.37E+04	1.20E-11
GNR10	1.52E-11	2.31E+04	1.19E-11

The translational diffusion coefficients from DLS and AUC are in good agreement. AUC however underestimates the translational diffusion coefficient, presenting systematically smaller values for every sample and hence predicting larger sizes. This deviation might be influenced by DLS and AUC measuring differently weighted averages of the rod size distribution.

References

[1] Olmon, R. L.; Slovick, B.; Johnson, T. W.; Shelton, D.; Oh, S.-H.; Boreman, G. D.; Raschke, M. B. Optical dielectric function of gold. *Physical Review B* **2012**, *86*, 235147.

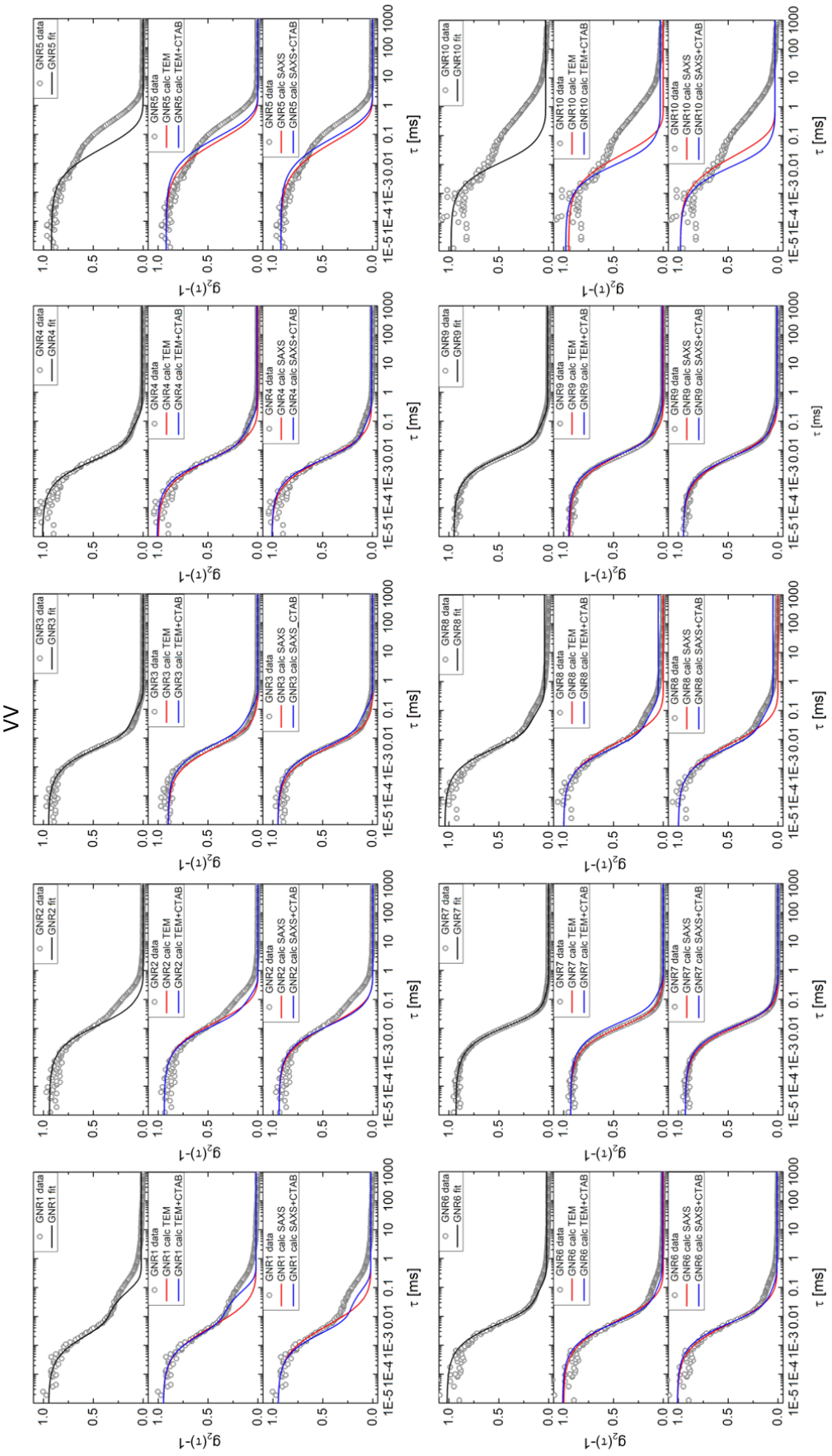

Figure S2: Polarised (VV) correlation functions of the scattered intensity $g_2(\tau)$ as a function of decay time τ for all gold nanorod samples GNR1 to GNR10. Top: DLS data (grey circles) with best nonlinear least-square fit (black). Middle: DLS data (grey circles) with calculated curves from TEM values for length and width (red) and with added CTAB shell (blue). Bottom: DLS data (grey circles) with calculated curves from SAXS values for length and width (red) and with added CTAB shell (blue).

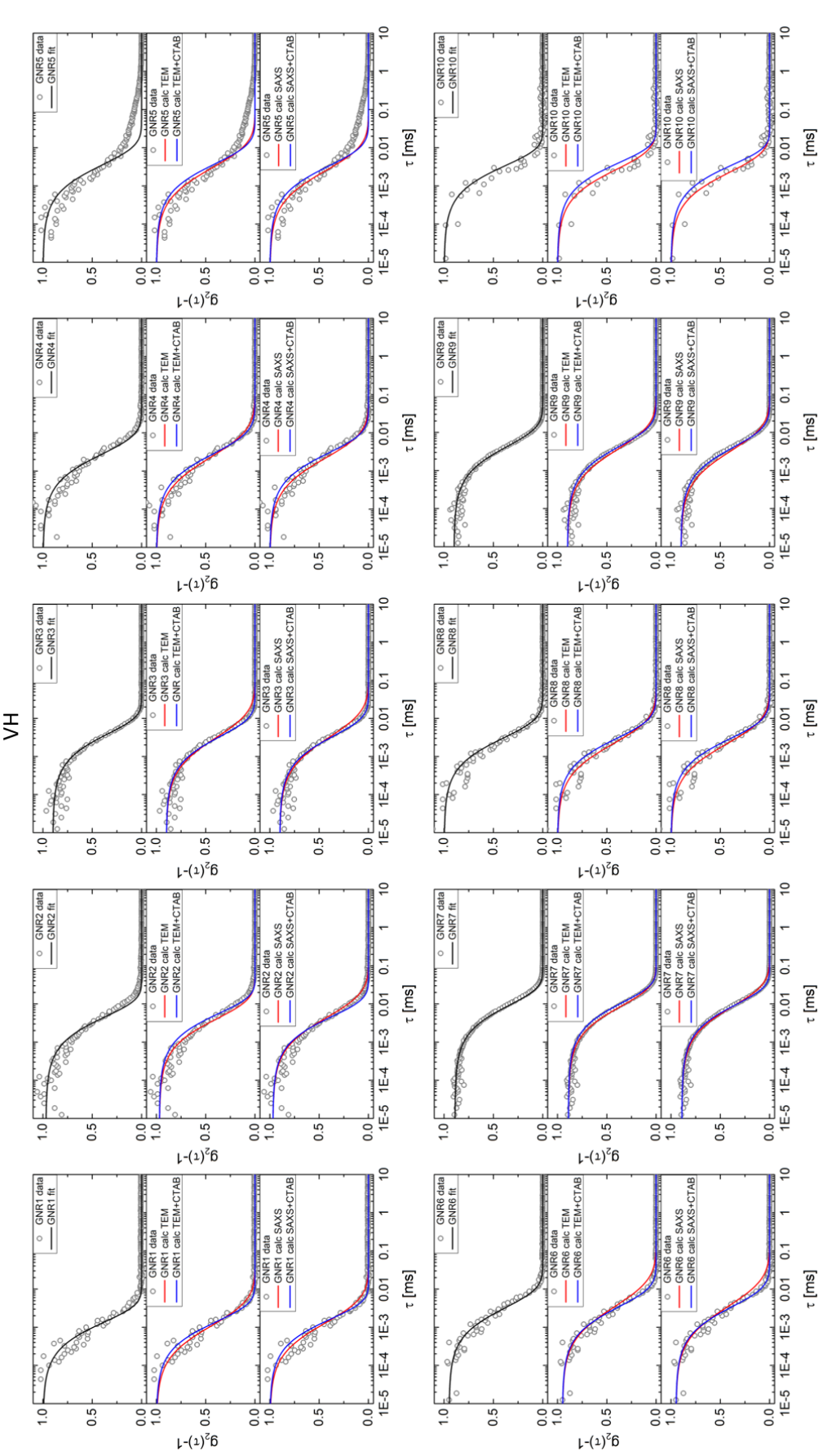

Figure S3: Depolarised (VH) correlation functions of the scattered intensity $g_2(\tau)$ as a function of decay time τ for all gold nanorod samples GNR1 to GNR10. Top: DLS data (grey circles) with best nonlinear least-square fit (black). Middle: DLS data (grey circles) with calculated curves from TEM values for length and width (red) and with added CTAB shell (blue). Bottom: DLS data (grey circles) with calculated curves from SAXS values for length and width (red) and with added CTAB shell (blue)

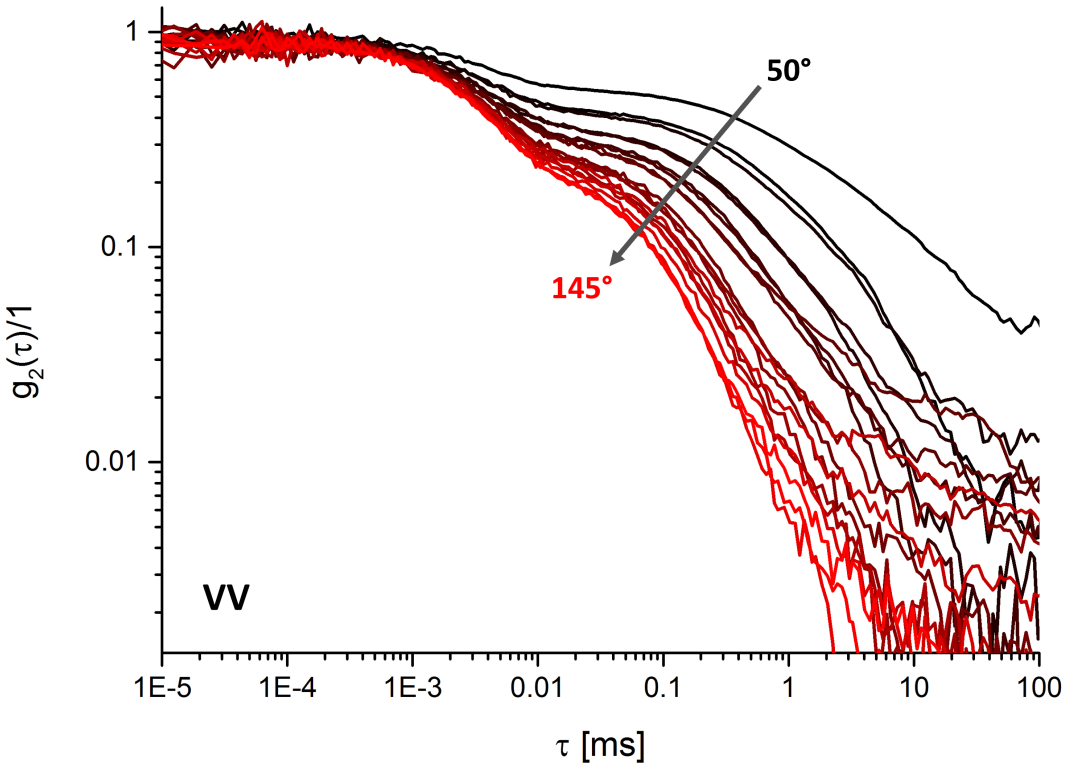

Figure S4: Angle dependent polarised (VV) correlation function of sample GNR1.

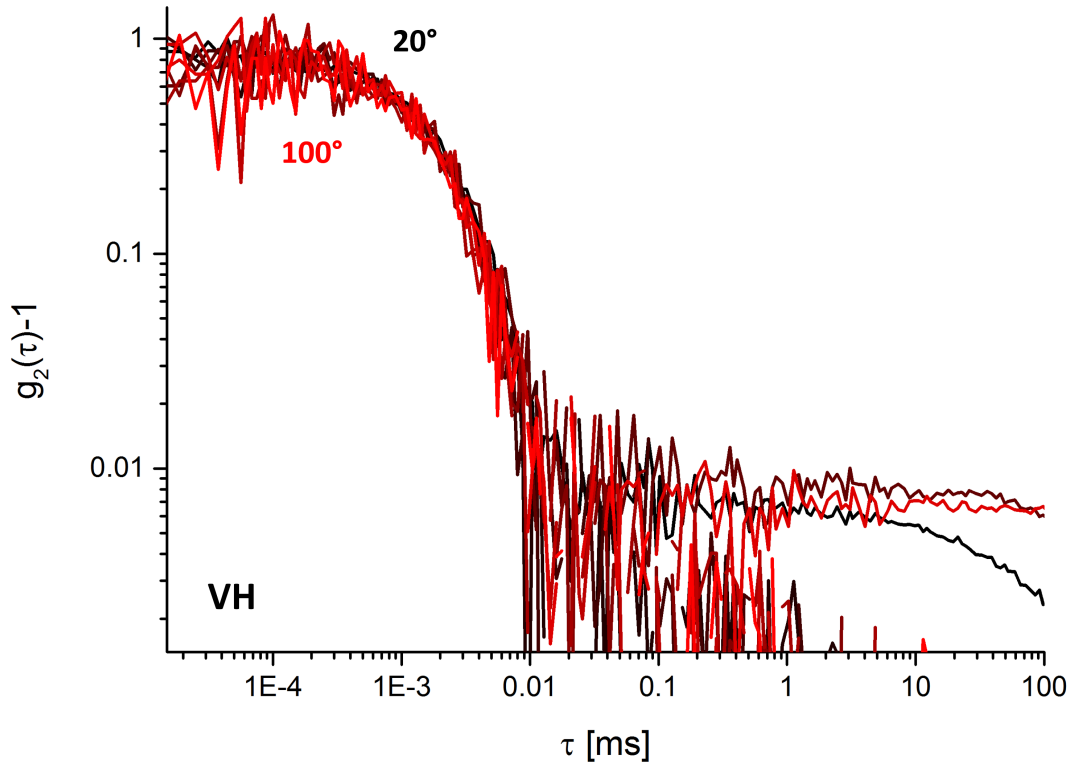

Figure S5: Angle dependent depolarised (VH) correlation function of sample GNR1.

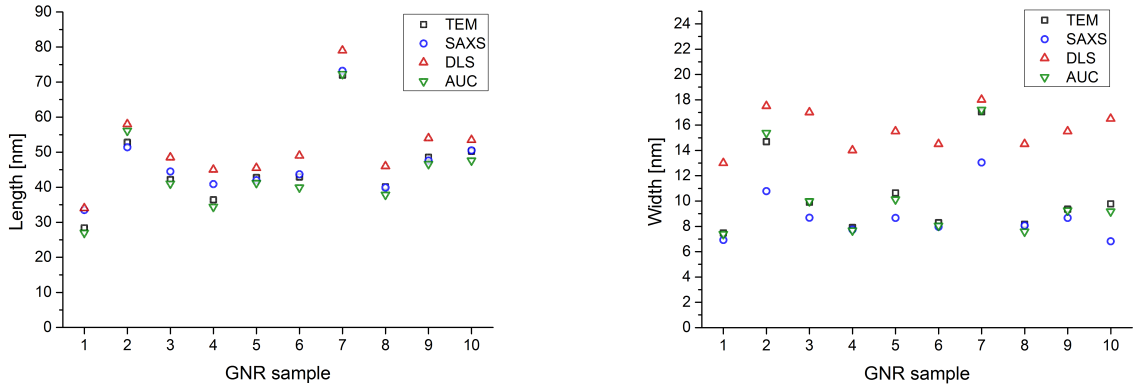

Figure S6: Visualisation of Table S3 for the length (left) and width (right) from all techniques for all 10 GNR samples.

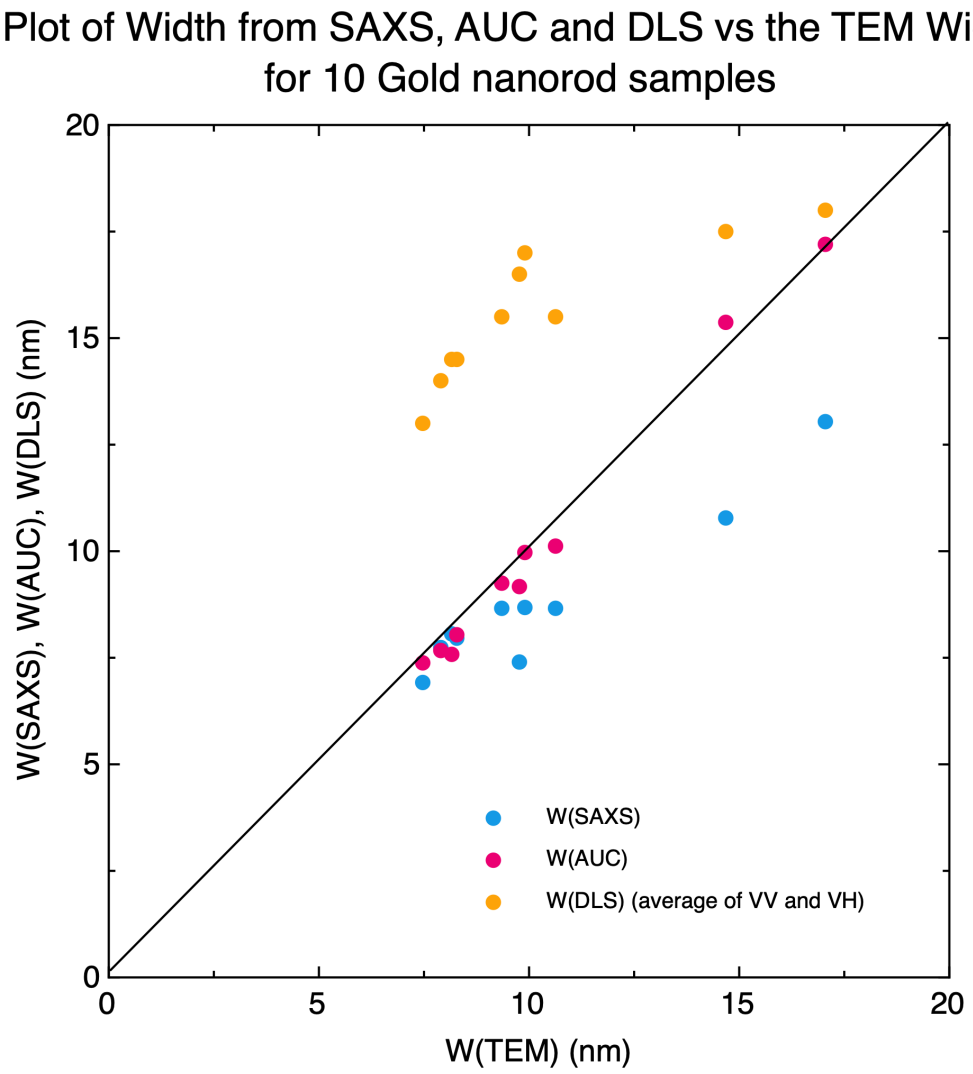

Figure S7: Plot of the Width of the gold nanorods measured by SAXS, DLS and AUC vs the width measured by TEM.)

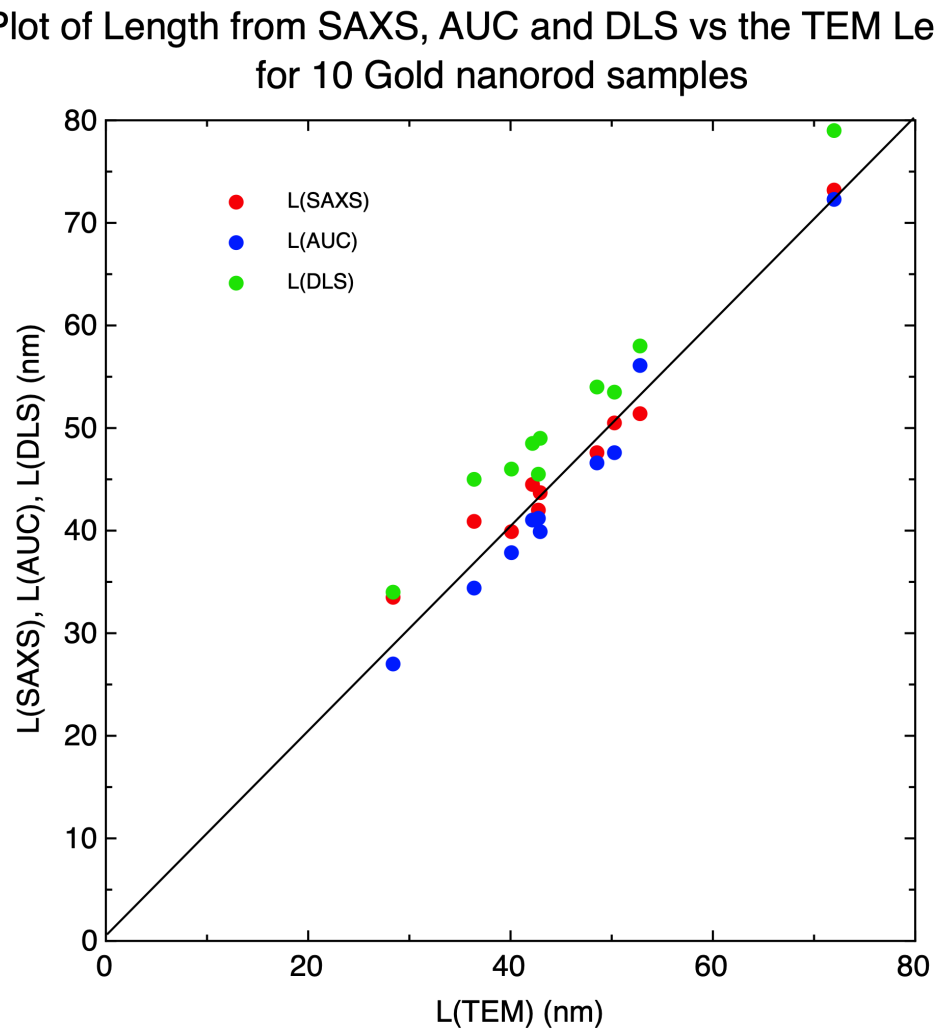

Figure S8: Plot of the Length of the gold nanorods measured by SAXS, DLS and AUC vs the width measured by TEM.)

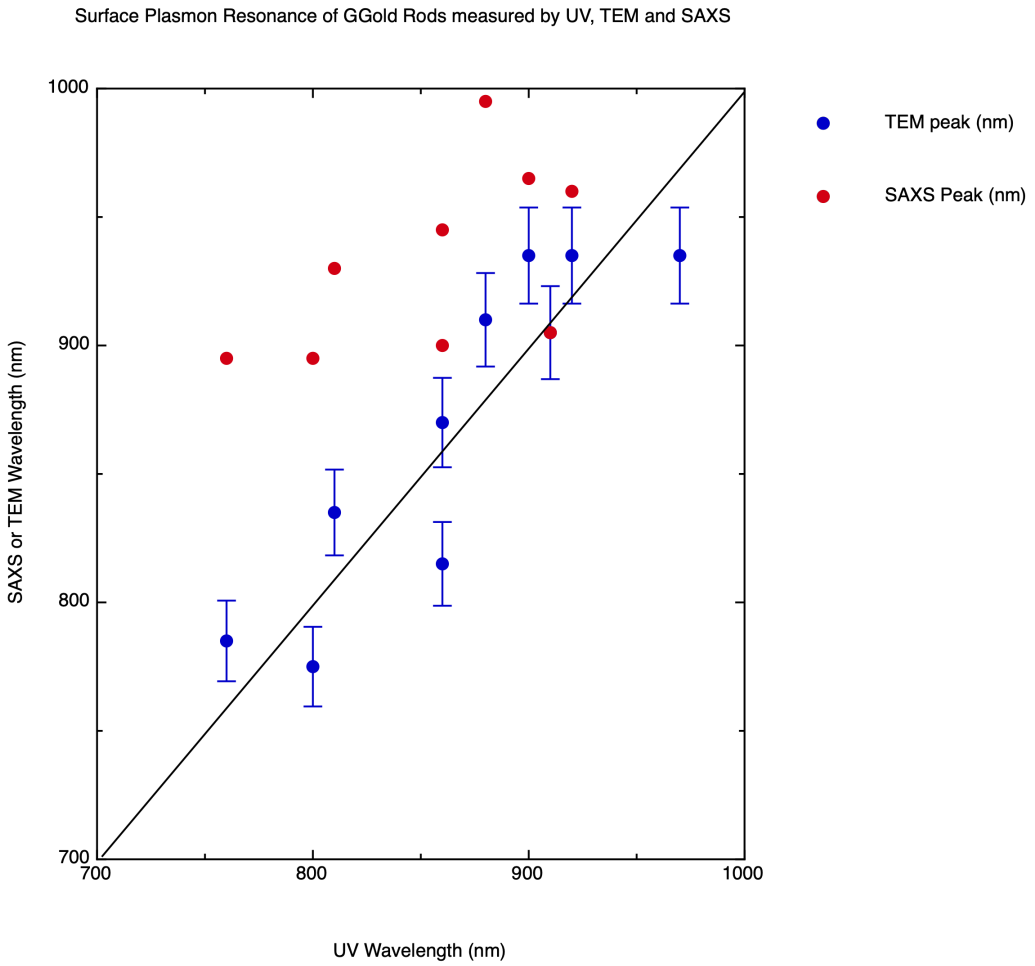

Figure S9: Plot of the predicted LSPR peak using SAXS and TEM as a function of the experimental position measured by absorption spectroscopy.)